Activation of diffuse discontinuities and folding of sedimentary layers

Martin Guiton, Yves Leroy, William Sassi

To cite this version:

Martin Guiton, Yves Leroy, William Sassi. Activation of diffuse discontinuities and folding of sedimentary layers. Journal of Geophysical Research : Solid Earth, 2003, 108 (B4), pp.1-20. ⟨10.1029/2002JB001770⟩. ⟨hal-00111388⟩

HAL Id: hal-00111388
https://hal.science/hal-00111388v1

Submitted on 20 Apr 2024

Activation of diffuse discontinuities and folding of sedimentary layers

Martin L. E. Guiton
Institut Français du Pétrole, Rueil-Malmaison, France

Yves M. Leroy
Laboratoire de Mécanique des Solides, Ecole Polytechnique, Palaiseau, France

William Sassi
Institut Français du Pétrole, Rueil-Malmaison, France

Folding of sedimentary layers is often accommodated by the opening or sliding of inherited and new discontinuities which are assumed here to be diffuse so that a continuum description applies at the fold scale. The rock rheology is then described with an elastoplasticity model for which the permanent deformation is of simple shear (sliding) or dilation (opening) with respect to specific orientations of the new or inherited diffuse discontinuities. To illustrate the relation between folding and activation of diffuse discontinuities, a three-dimensional layer under compression in the two horizontal directions and sustaining the overburden lithostatic pressure is studied. Cylindrical buckling occurs either before (elastic) or after the diffuse discontinuities have been activated. If buckling is elastic, inherited vertical discontinuities, striking obliquely to the fold geometrical axes, are activated in a sliding mode in the outer arc, leading to a rotation of the principal stress directions. Opening is then detected across new vertical planes striking obliquely to the fold axis. The activation of inherited or new vertical discontinuities can be suppressed if sliding takes place along weak bedding interfaces. Alternatively, early and homogeneous layer-parallel shortening, marked by a reverse fault mode, drastically reduces the critical buckling load compared to the Euler load and modifies the final geometry of buckling which is then more of a circular dome shape. The switching in buckling mode results in the fold limbs in a change from the early reverse fault to a strike-slip fault sliding and to opening across diffuse planes oriented consistently with the final circular structure.

1. Introduction

[2] The objective of this paper is to analyze the coupling between the activation of inherited or new discontinuities and the development of a three-dimensional fold. This investigation is part of a research program aimed to the prediction of fracture densities and orientations in folded sedimentary layers.

[3] Predicting structural instabilities such as folding requires the selection of appropriate rheological models for the deforming rocks, and thus the identification of the relevant deformation mechanisms. For salt in sedimentary basins and more generally for rocks in the lithosphere, a linear or power law creep law is most appropriate and the rheological parameters can be estimated from laboratory measurements (see *Carter and Tsenn* [1987] for a review of experimental results and examples of deformation maps). Folding is then predicted on length scales ranging from centimeter scale [*Sherwin and Chapple*, 1968] to that of the lithosphere thickness [*Martinod and Davy*, 1992; *Cloething et al.*, 1999], following a method which is due essentially to the seminal work of *Biot* [1965]. For folding at the lithospheric scale, it has been recognized that the pervasive fracturing of the upper crust should modify the bending stiffness of the structure studied [*McAdoo and Sandwell*, 1985]. This idea was explored by *Wallace and Melosh* [1994], who accounted for a population of frictionless

faults. An alternative approach consists of smearing these faults over a representative volume element, such that a continuum approximation and an elastoplasticity model become applicable. The information usually lost during the averaging is the preferential orientation of the discontinuities predating the tectonic event studied. The objective of this paper is to palliate to this deficiency and to study folding in the presence of inherited weak orientations, with the application of the plasticity model presented by *Leroy and Sassi* [2000]. This model provides a simple description of the contribution of fractures to the macroscale irreversible deformation.

[4] The development of a rheological model to describe the response of a representative volume element containing planar defects such as cracks has received a lot of attention in the geophysical community, as well as in various branches of engineering. *Walsh* [1965] considered circular cracks in dilute concentration while *Budiansky and O'Connell* [1976] started from elliptical cracks and accounted for interaction with a self-consistent scheme. Friction along the crack faces was described by *Kachanov* [1982a], and in the three above studies, effective elastic properties were derived. Accounting for crack growth if the loading is partly in mode II renders any modeling difficult because of branching [*Kachanov*, 1982b]. If a homothetic mode of growth remains however relevant, then a model for frictional cracks with increase in both density and defect size has been proposed [*Gambarotta and Lagomarsino*, 1993].

[5] The rheological models discussed above are already complex despite the selection of simple microscale mechanisms and the assumption of linear elasticity. Field observations reveal a variety of deformation mechanisms on a length scale where the material is heterogeneous. This remark explains why simpler rheological models should be first considered for nonlinear folding analyses at the kilometer scale. The main feature, which should be retained by these simplified models, is that the material response is anisotropic, due to the presence of inherited weak orientations. A short review of this class of models is given by *Leroy and Sassi* [2000]. The averaging method often employed is reminiscent to the one proposed by *Batdorf and Budiansky* [1949] for computing the effective properties of an assembly of monocrystals, each contributing by slip to the irreversible macroscale deformation. If the resulting rheological law is an elastoplasticity model, it can usually be cast into the general framework proposed by *Koiter* [1953] for multiple yield surfaces.

[6] Enriching a constitutive law with the description of the microscale dissipative mechanisms usually leads to a reduction of the predicted critical stress magnitude for the onset of instability either in a shear band mode [*Rudnicki and Rice*, 1975] or in a structural mode such as necking [*Stören and Rice*, 1975]. This sensitivity is often assessed with a simplified plasticity theory referred to as a deformation theory, which mimics the presence of sliding microcracks for the case of frictional materials. The reader is referred to *Leroy and Triantafyllidis* [2000] for further discussion. For example, it has been shown that the critical load at the onset of buckling for a prototype of a cross section through the Campos basin (Brazilian continental margin) could be reduced by a factor of 5, to a magnitude consistent with the sedimentary compressive loading, if a deformation theory was applied [*Triantafyllidis and Leroy*, 1997]. The nonlinear development of the instability requires however a complex elastoplasticity model based on a description of the microscale dissipative mechanisms. The rheological model of *Leroy and Sassi* [2000] is constructed from such a description and, once amended to account for finite rotations [*Guiton*, 2001], should thus permit to capture the development of buckling in the presence of inherited weak orientations.

[7] The paper contents are as follows. Section 2 is concerned with the constitutive relations adopted for the pervasively fractured rock. The elastoplasticity model is motivated by comparing the incremental stress-strain response with the macro-stress-strain relation based on linear elastic fracture mechanics, for a representative volume element containing frictional, penny-shaped cracks. The details of the numerical algorithm for the elastoplasticity constitutive relations are found in Appendix B. Sections 3–6 present the numerical results for the buckling of a layer buried at 1 km and sustaining unequal compressions in the two horizontal directions. The weak formulation of the mechanical equilibrium at the basis of the finite element approximation is found in Appendix A. Sections 3 and 4 are concerned with the elastic solution and the role of inherited pervasive discontinuities which are either vertical or horizontal, and activated in sliding only. In section 5, new orientations, which are partly controlled by the sliding of the previously discussed inherited discontinuities, are found to be activated in an opening mode during folding. In section 6, the rock is assumed to be poorly consolidated so that sliding occurs prior to buckling in a conjugate reverse fault mode. This early activation reduces drastically the buckling load and leads ultimately to a change from an essentially cylindrical to a circular shape fold. This evolution leads to the deactivation of the prefolding fracture pattern and to the sliding along and opening across new orientations in the fold limbs which are documented.

2. Constitutive Relations

[8] The first objective of this section is to summarize the plasticity model of *Leroy and Sassi* [2000], and the second is to compare the corresponding stress rate–strain rate relations with those obtained for an elastic solid containing penny-shaped frictional cracks. This comparison provides an interpretation for the plasticity model parameters in terms of crack density, crack size and frictional properties.

[9] The comparison starts from the description of a rock mass, defining the representative volume element (RVE) of interest, which is pervasively transgressed by inherited planar defects (Figure 1a). These inherited discontinuities could be for example, vertical joints or horizontal surfaces marking the separation of two rock sequences. They are weak in the sense that their toughness is less than the fracture toughness of the surrounding rock. During deformation of the rock mass, every discontinuity, defined by its normal **n** with the two Euler angles θ_1 and θ_2 (Figure 1b), responds to the mechanical loading independently. This response is either of a perfect stick (no activation) or

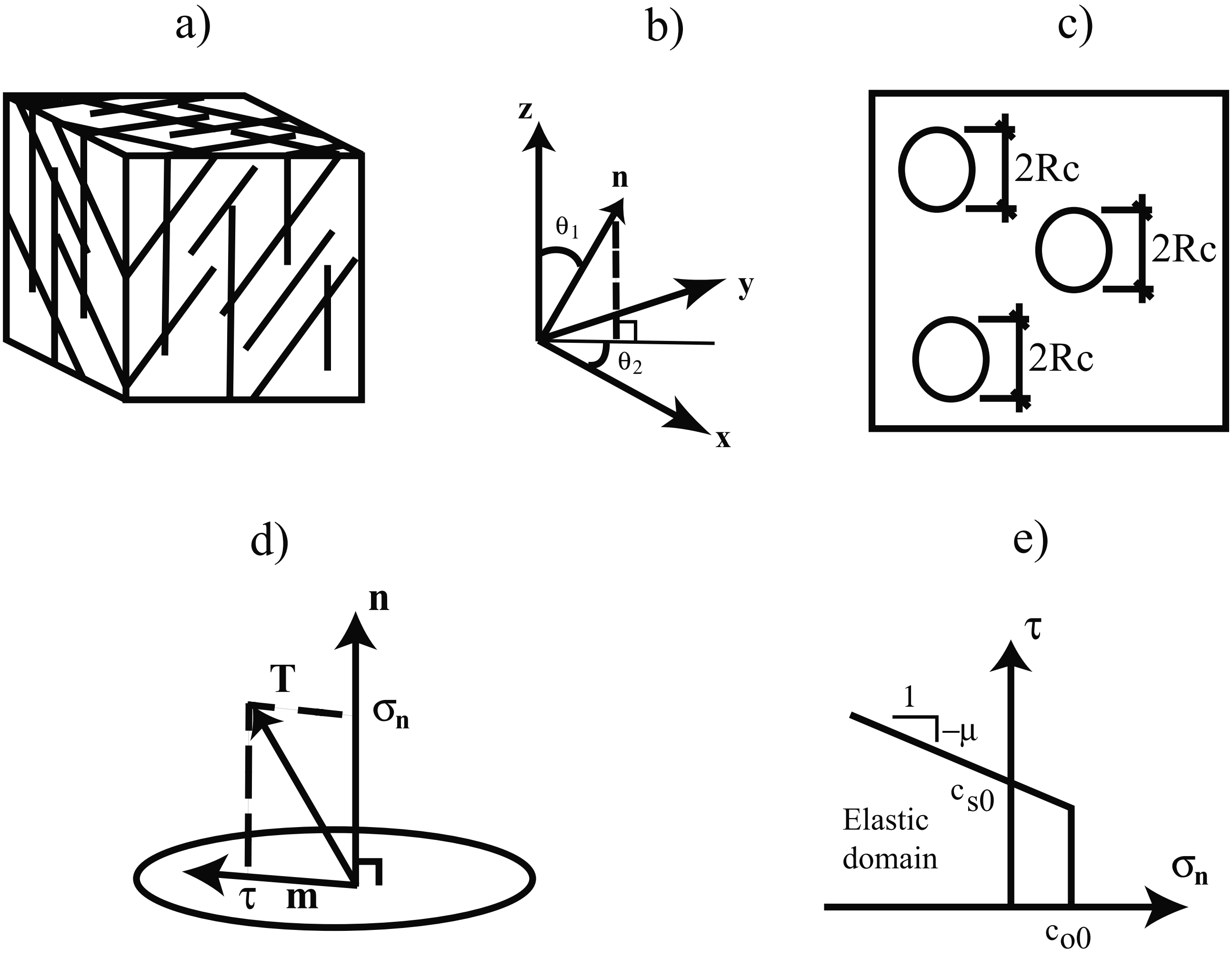

Figure 1. The micromechanisms motivating the constitutive model. (a) The representative volume element (RVE) is pervasively transgressed by inherited planar discontinuities. (b) A set of parallel fractures with normal **n** is defined by the two Euler angles θ_1 and θ_2. (c) Penny-shaped patches on a given plane with same radius R_c are considered as cracks accommodating sliding and opening. (d) The components of the stress vector **T** applied on a patch of normal **n**. (e) The truncated Mohr-Coulomb criterion used to detect the sliding and opening along a given planar surface; μ, c_{S0} and c_{O0} are the friction coefficient, the cohesion, and the tensile strength, respectively.

of a discontinuity (jump) in displacement, in a direction parallel or perpendicular to the plane defining the activation in sliding or opening, respectively.

[10] The construction of a rheological model for the rock mass described above requires further assumption on the microstructure. For example, one could envision that the jumps in displacement occur over isolated patches assuming, for simplicity sake, that all patches on a given plane have a penny shape and the same radius R_c (Figure 1c). The total number of patches over all surfaces having the same normal **n** and transgressing the RVE is $P(\mathbf{n})$, such that the crack density $\Phi(\mathbf{n})$ is $P(\mathbf{n})R_c^3(\mathbf{n})/V$, in which V is the volume of the RVE. Note that bold letters are reserved for vectorial or tensorial quantities in this paper. The mechanical response of every crack is independent of neighboring patches, requiring this density to be small compared to one or their distribution to be random [*Kachanov*, 1992]. In that instance, the exact solution of a penny-shaped crack in an infinite medium can be considered to relate jumps in displacement at the patch scale to the remote macrostress (Figure 1d). These various assumptions permit to make the distinction between macroscale and microscale in this paper.

[11] Consider an isolated penny-shaped crack of normal **n** in an isotropic elastic medium (characterized by the modulus of elasticity E and Poisson's ratio ν), where the stress state $\boldsymbol{\sigma}$ prevails at infinity. The displacement jump across the two faces of the crack averaged over its surface is denoted **b** and is given by

$$\mathbf{b}(\mathbf{n}, \boldsymbol{\sigma}) = \mathbf{T} \cdot \mathbf{B}(\mathbf{n}, \boldsymbol{\sigma}) \quad \mathbf{T} = \boldsymbol{\sigma} \cdot \mathbf{n}, \tag{1}$$

in which **T** and **B** are the stress vector and the crack compliance second-order tensor. The center dot in equation (1) and in what follows, between, for example, any two second-order tensors **A** and **B**, designates the product: $\mathbf{A} \cdot \mathbf{B} = A_{ij}B_{jk}\mathbf{e}_i \otimes \mathbf{e}_k$ in an orthonormal basis $\{\mathbf{e}_i\}$ and with $\otimes$ identifying the tensorial product ($\mathbf{A} = A_{ij}\mathbf{e}_i \otimes \mathbf{e}_j$).

Summation is implied by repeated indices. The tensor **B** is defined by

$$\mathbf{B}(\mathbf{n},\boldsymbol{\sigma}) = b_O R_c \mathbf{n}\otimes\mathbf{n} + b_S R_c(\boldsymbol{\delta} - \mathbf{n}\otimes\mathbf{n} + \mu\mathbf{n}\otimes\mathbf{m}),$$
$$b_O = \frac{16(1-\nu^2)}{3\pi E} \quad b_S = \frac{2b_O}{(2-\nu)}, \tag{2}$$

in which **δ**, **m** and μ are the second-order identity tensor ($\mathbf{e_i} \otimes \mathbf{e_i}$), the unit vector in the direction of the tangential component of the stress vector (see Figure 1d), and the friction coefficient between the crack faces, respectively. Relations (1) and (2) are given by *Kachanov* [1992] except for the modification of the compliance tensor to account for the frictional properties of the crack. This modification consists of replacing the resolved shear stress τ ($\tau = \mathbf{T}\cdot\mathbf{m}$) by the equivalent stress $\tau + \mu\sigma_n$ ($\sigma_n = \mathbf{n}\cdot\mathbf{T}$ is the normal stress), as discussed by *Bui* [1978] and *Kachanov* [1982a]. The expression for b_O and b_S in equation (2) are classical in fracture mechanics and could be derived directly from *Eshelby*'s [1957] results as by *Budiansky and O'Connell* [1976]. The average strain ε over the RVE is then found to be

$$\boldsymbol{\epsilon} = \mathbf{C}^e : \boldsymbol{\sigma} + \sum \frac{\pi\Phi(\mathbf{n})}{R_c}\frac{1}{2}(\mathbf{b}(\mathbf{n},\boldsymbol{\sigma})\otimes\mathbf{n} + \mathbf{n}\otimes\mathbf{b}(\mathbf{n},\boldsymbol{\sigma})), \tag{3}$$

in which $\mathbf{C}^e$ is the elastic compliance of the rock mass, a fourth-order isotropic tensor based on Hooke's law (its inverse, the elastic stiffness, is defined in Appendix B). The sum in equation (3) is over all orientations transgressing the RVE. Introducing the expression for the average displacement (equation (2)) in equation (3) provides an expression for the macrostrain explicitly in terms of the macrostress

$$\boldsymbol{\epsilon} = \mathbf{C}^e : \boldsymbol{\sigma} + \sum \pi\Phi(\mathbf{n})\Big(b_O\sigma_n\mathbf{n}\otimes\mathbf{n} + b_S(\tau+\mu\sigma_n) \cdot \frac{1}{2}(\mathbf{n}\otimes\mathbf{m} + \mathbf{m}\otimes\mathbf{n})\Big). \tag{4}$$

This relation (4), presented without discussing the stress conditions for crack opening ($\sigma_n > 0$) and sliding ($\tau + \mu\sigma_n \geq 0$ and $\sigma_n \leq 0$) nor the stress path dependence, defines the effective elastic properties of the REV.

[12] These effective elastic properties have been studied extensively in the past and the reader is referred to *Kachanov* [1992] for a critical review. For example, accounting for the potential crack branching permits to estimate the medium dilatancy induced by sliding [*Kachanov*, 1982b; *Horii and Nemat-Nasser*, 1986; *Jeyakumaran and Rudnicki*, 1995]. Of more interest here is the evolution of the patch density, of the size of the patches and of the sliding along the crack faces. For that purpose, one could assume homothetic growth, preserving the simplicity of the micromechanism description. The implied in-plane growth under mode II loading would then require that the in-plane fracture toughness is less than in the bulk. The evolution of the microstructure is of course anisotropic and requires to check simultaneously crack growth and sliding criteria with a rate formulation [*Gambarotta and Lagomarsino*, 1993]. This approach is certainly complete but too complex to motivate its immediate use in the three-dimensional structural analysis considered here.

[13] It is for that reason that an elastoplasticity model is preferred. The permanent macrodeformation is constructed from the contribution of independent orientations of fracture planes [*Leroy and Sassi*, 2000]. The elastic properties of the RVE are the same as the ones of the matrix and the deformation resulting from the cracks activation is reproduced by the irreversible or permanent deformation. Two yield criteria are proposed to check the activation of a given orientation:

$$\phi_S(\boldsymbol{\sigma},\mathbf{n},\gamma) \equiv \tau + \mu\sigma_n - (c_{S0} + c_{S1}\gamma) \leq 0$$
$$\phi_O(\boldsymbol{\sigma},\mathbf{n},d) \equiv \sigma_n - (c_{O0} + c_{O1}d) \leq 0, \tag{5}$$

corresponding to the sliding and the opening mode, respectively. In equation (5), the scalars c_{S0}, c_{O0}, c_{S1}, c_{O1}, γ, and d are the cohesion, the tensile strength, the hardening moduli in sliding and opening, and two internal variables which marks the accumulated macrodeformation in sliding and in opening, respectively. The cohesion and the tensile strength are defined in Figure 1e and could be estimated in laboratory tests. The other four parameters could be given a physical interpretation in terms of the crack density of the elastic solid defined above. Note before doing so that the consistency conditions of the yield criteria in equation (5) ($\dot{\phi}_S = 0$, $\dot{\phi}_O = 0$) provide two relations between the evolution in stress and in the internal variables: $\dot{\tau} + \mu\dot{\sigma}_n = c_{S1}\dot{\gamma}$ and $\dot{\sigma}_n = c_{O1}\dot{d}$, which characterize the linear hardening law introduced above. Note also that the positive hardening for the opening mode necessitates to imagine that opening is coeval to an infill of the fractures, for example, due to a mineralization, a fact often observed in the field [*Jamison*, 1997]. The rate form of the stress-strain relation for the elastoplasticity model reads

$$\dot{\boldsymbol{\epsilon}} = \mathbf{C}^e : \dot{\boldsymbol{\sigma}} + \sum\Big(\dot{d}\mathbf{n}\otimes\mathbf{n} + \dot{\gamma}\frac{1}{2}(\mathbf{n}\otimes\mathbf{m} + \mathbf{m}\otimes\mathbf{n})\Big), \tag{6}$$

in which the two basic modes of deformation are uncoupled. We are now in a position to provide a simple interpretation for the linear hardening moduli c_{S1} and c_{O1}. For that purpose, take the time derivative of the stress-strain relation in equation (4), assuming the stress evolution leaves the vector **m** unchanged. Furthermore, consider the crack density constant in time and compare the rate form of equation (4) with equation (6) to conclude that

$$c_{S1}\pi b_S\Phi(\mathbf{n}) \sim 1 \quad c_{O1}\pi b_O\Phi(\mathbf{n}) \sim 1. \tag{7}$$

[14] The hardening moduli are inversely proportional to the crack density times the scalar b_S or b_O, defined in equation (2). These moduli are positive and, if assumed constant, imply that the crack population is not changing with the accumulated deformation. Relation (7) is nevertheless proposed to motivate why low hardening moduli are considered for weak inherited directions (large fracture densities) and large moduli for new directions (low density of preexisting flaws). This difference between inherited weak orientations and new orientations is of course valid

if the same kinematics of the irreversible deformation presented in equation (6) is adopted for both, as suggested by *Leroy and Sassi* [2000]. This is exactly the assumption which is made in the folding simulations presented next: different rheological parameters are considered to differentiate between inherited and new orientations. It should be stated finally that relation (7) will not be used to quantify the hardening moduli in section 3 based on the fracture densities found in the field [e.g., *Renshaw*, 1997]. Such predictions would render the material too stiff and the stress changes during folding unrealistic. A complete discussion of the deformation mechanisms related to the natural fractures is beyond the scope of the present paper and is deferred to future work.

3. Preliminary: The Elastic Solution

[15] The two simulations reported in this section concern the elastic solution for a perfect and an imperfect structure. The material is linearly isotropic elastic with Young's modulus E and Poisson's ratio ν set to 5 GPa and 0.2, respectively. Sections 4-6 explore the development of fracture patterns. The boundary value problem is the same for all simulations and is first described next.

[16] The initial geometry consists of a plate having a square top surface $2L \times 2L$ ($L = 2$ km) and a thickness h of 200 m (Figure 2a). The plate midsurface is at a depth of 1 km. We assume a volumetric mass of 2200 kg/m^3 everywhere. The vertical principle stress σ_v is calculated from the lithostatic gradient. It equilibrates the action of the overburden and of the substratum on the plate, which are assumed to be fluid-like, resulting in lithostatic pressures along the inward normal of the top and bottom surfaces, respectively. The horizontal principal stresses are set to $0.9\sigma_v$.

[17] Loading in time results from two compressions, the first obtained by controlling a horizontal uniform x displacement denoted δ on the lateral surface at $x = 2$ km, while constraining the opposite surface at $x = -2$ km from any motion in the x direction. The orientation of the coordinate system is provided in Figure 2 with the x axis directed to the north and with origin at the geometrical center of the plate. The second compression results from a similar displacement control in the y direction over the lateral surfaces at $y = \pm 2$ km, with a magnitude set to 0.7δ. Two points, with coordinates ±2, 0, 0 (km), have their vertical displacement set to zero, to avoid arbitrary vertical translation. To trigger buckling, a perturbation in the initial geometry is introduced by adding to the z coordinate the quantity $A[1 + \cos(\pi x/L)][1 + \cos(\pi y/L)]$ with an amplitude A set to 10 cm. The plate is discretized with 243 or 300 Lagrange elements having each 27 nodes. There are three elements through the thickness of the plate to capture the stress gradients with depth prevailing during buckling.

[18] Figure 3 presents the evolution of the load P which is work conjugate to the displacement δ prescribed over two of the lateral boundaries. This P–δ curve labeled 1 is the elastic solution for a perfect structure. Curve 2 is obtained in the presence of the initial imperfection described above. The magnitude of the imperfection is small enough compared to the plate thickness to ensure that the Euler load P_E is well approximated by the point at which these two curves are seen to separate. Note that the load keeps on increasing with the displacement signaling that the elastic buckling is stable. The shape of the emerging fold is plotted in Figure 2 at three load levels denoted P_1, P_2, and P_3 in Figure 3. Isocontours of the vertical displacement (km) are plotted over the fold current configuration. Load P_1 is approximately 73% of the Euler load and the gradient in vertical displacement is minor (15 m over 2 km). Load P_2 is slightly larger than P_E (106%), and the emerging fold has a rather cylindrical shape with axis parallel to the y direction. It is only in the latest stage of the fold development (load P_3 is 120% P_E) that the fully 3-D nature of the kinematics is clearly seen. Note by comparing the fold at P_2 and P_3 that the point of largest altitude is not always at the center of the plate since it evolves from the side at $y = \pm 2$ km to the center, as the load is increased from P_2 to P_3.

[19] It is now proposed to make use of the stress shape factor R to analyze the evolution of the stress state during folding. This factor is defined as the principal stress ratio $R = (\sigma_2 - \sigma_3)/(\sigma_1 - \sigma_3)$, with the continuum mechanics convention that stresses are positive in tension and the ranking: $\sigma_1 \geq \sigma_2 \geq \sigma_3$. R is varying from 0 to 1 and is presented in the inner circle of Figure 4, for the six possible orientations of the principal stresses. The stress shape factor does provide some insight on the potential mode of failure defined by the type of faulting or jointing first activated [*Sibson*, 1985; *Sassi et al.*, 1993; *Sassi and Faure*, 1997]). It was first considered by *Wallace* [1951] and *Bott* [1959] to infer the slip direction along faults. The three failure modes presented on the right of Figure 4 correspond to reverse fault (compression), strike-slip and normal fault (extension) for a vertical σ_1, σ_2, and σ_3, respectively. The left-hand side of Figure 4 corresponds to a rotation by 90° of the two horizontal principal stresses, as can be judged by the stereonet diagrams with Schmidt projection on the lower hemisphere (same convention for all stereonets in what follows). These stereonets illustrate the orientation of the normals to potential failure planes, based on a Mohr-Coulomb criterion with a friction angle of 25° and a R of 0.5. To distinguish between the three failure mode sectors in the right- or left-hand side of Figure 4, the R^* stress factor is now introduced on the outer circle and is constructed to vary continuously from 0 to 3. The ranges of 0 to 1 (dark blue to blue colors), one to two (blue to light green colors) and 2 to 3 (light green to red colors) corresponds to the compression, strike-slip and extension failure mode, respectively.

[20] The stress distribution for the elastic solution is now analyzed by plotting the stress shape factor R^* on the current configuration of the fold at the three loading stages discussed above (Figures 5–7). The isocontours of R^* are plotted in two views, the first looking at the plate from above and the second from underneath. To complete these data, the values of the principal stresses are provided at a few representative sites together with their orientations in stereonet diagrams. Circles, triangles, and squares are used to identify σ_1, σ_2, and σ_3 directions, respectively.

[21] Figure 5 provides the two views of the structure at load P_1, which is less than the Euler load. The principal stresses have the same orientation over the whole domain with the maximum stress (σ_1, circles) being vertical. The principal stress along the dominant compressive direction in

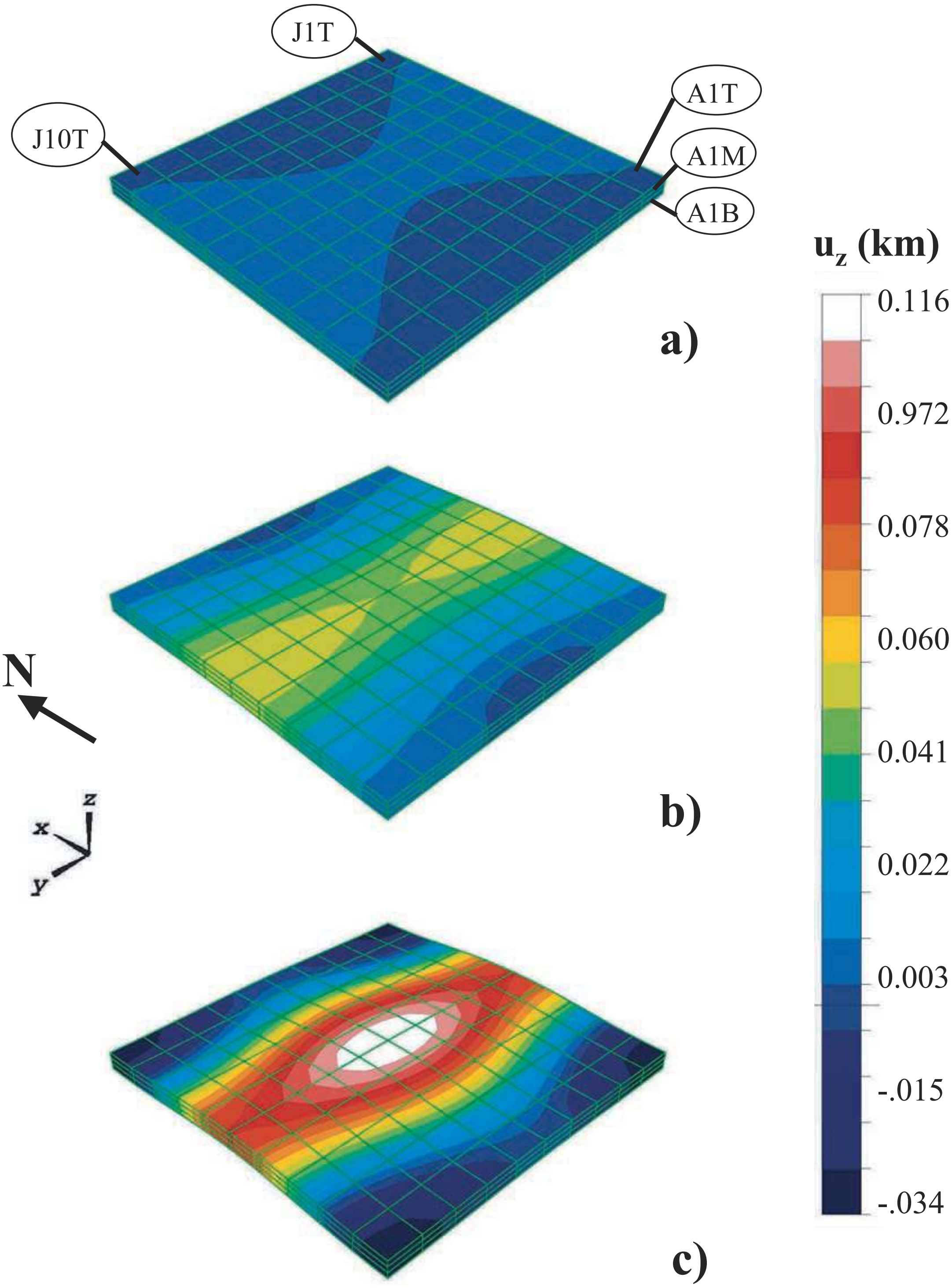

Figure 2. Isocontours of the vertical displacement (km) over the elastic structure. The isocontours are plotted (a) prior to buckling, (b) at its onset, and (c) at the end of the simulation in. The load at these three instants are P_1, P_2, and P_3 defined in Figure 3.

the x direction (north) is minimum (σ_3, squares). The intermediate stress (σ_2, triangles) is along the minor compressive direction which is the y direction. The two compressions in the horizontal directions have already modified the stress regime from the initial extension regime. The magnitude of the minimum stress has a gradient, mainly in the x direction, over both the top and bottom surface. This is the first expression of the development of the perturbation responsible ultimately for buckling. This gradient partly explains the variation in R^* from 0.1 to 0.35. Such values reveal that the expected failure mode is in conjugate reverse faults striking along the y axis. The magnitude of the stress deviator, approximately 5 MPa, would require a friction coefficient lower than 0.3 to trigger faulting.

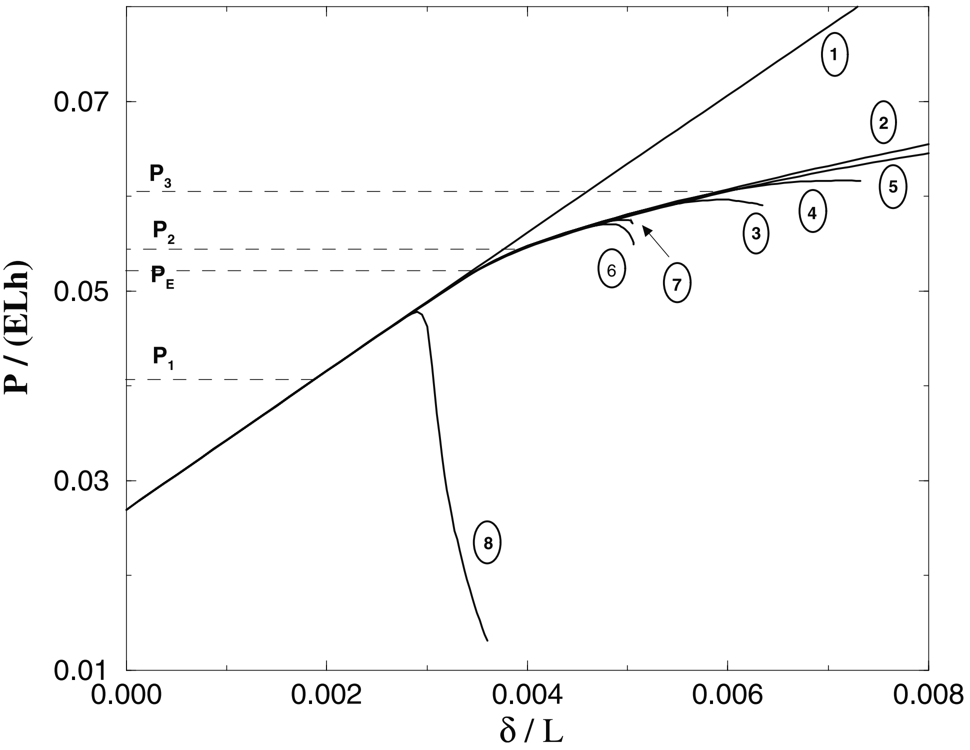

Figure 3. The force *P* is work conjugate to the displacement δ prescribed on the boundaries. The eight curves correspond to (1) the elastic fundamental solution; (2) the elastic imperfect structure; (3) a single set of systematic joints with θ_2 (defined in Figure 1b) set to 40° and sliding mode only; (4) a single set of systematic joints with $\theta_2 = 50°$ and sliding mode only; (5) a set of horizontal discontinuities plus a set of vertical systematic joints with $\theta_2 = 50°$; (6) new fractures plus a set of inherited joints with $\theta_2 = 50°$; (7) new fractures plus a set of inherited joints with $\theta_2 = 0°$; and (8) new fractures activated before buckling.

[22] Figure 6 presents the spatial variation of the stress shape factor R^* at load P_2 which is slightly larger than the Euler load. The principal stresses are still Andersonian with the maximum principal stress along the vertical direction. The intermediate and minor stresses are permuting in orientation over the domain. The stress shape factor is varying from 0 to 1.25 over the domain, indicating that the intermediate principal stress varies from the minimum horizontal principal stress to the vertical stress. R^* is close to 1 along the axis of the emerging fold in both the upper and lower outer arcs. The expected failure mode includes the reverse faulting discussed above as well as the strike-slip mode characterized by conjugate vertical faults for a stress shape factor greater than 1. The distribution of R^* correlates with the shape of the emerging fold (Figure 2b), which is rather two-dimensional, especially from the view of the top surface. The onset of buckling is sufficient to reduce in the outer arc the compression in the x direction, explaining the shift in principal stress directions in the horizontal plane, as can be seen from the values of the principal stresses presented in Figure 6.

[23] Figure 7 is constructed at load P_3, which corresponds to the latest stage of folding. The orientation of the principal stresses varies significantly over the domain. The maximum principal stress is not always vertical and is even found to be positive in the outer arc. This is clearly seen at the top of the anticline, element E6T. Please note that every element is identified with a set of two letters and a number, as illustrated in Figure 2a. The first letter ranges from A to J along the x axis, starting from the elements at $x = -2$ km. The integer ranges from 1 to 10 in the y direction. The second letter designates the depth at which the element is found and is either T, M, or B which stands for top, middle, or bottom, respectively.

[24] Looking first at the top view in Figure 7a, four stress regions should be distinguished. In the inner arcs (series of elements around AT and JT, $0.5 \leq R^* \leq 0.75$), the compression stress regime is the same as in Figure 5 with an increase in the stress deviator. Failure could be in conjugate reverse faults striking in the y direction. In the second region, corresponding to outer arcs at the structure boundaries (elements around D10T to G10T and D1T to G1T, $0.75 \leq R^* \leq 1.5$), the tensile stress calls for the opening of axial joints whereas the stress deviator could motivate a failure by strike-slip faulting. The third region is defined by the top center (elements such as F6T and E5T, $1.5 \leq R^* \leq 2$). Strike-slip failure mode is expected there but the proximity of the extension failure domain announces also the potential activation of joints. Note that strike-slip fault could be replaced by normal faults since the magnitude of the intermediate and minor principal stresses are rather close. The fourth region is what remains and is identified by the dark blue color ($0 \leq R^* \leq 0.5$). The main result in that region is that the two horizontal principal stress directions are not aligned with the compression directions. The magnitude of the two horizontal stresses (minor and intermedi-

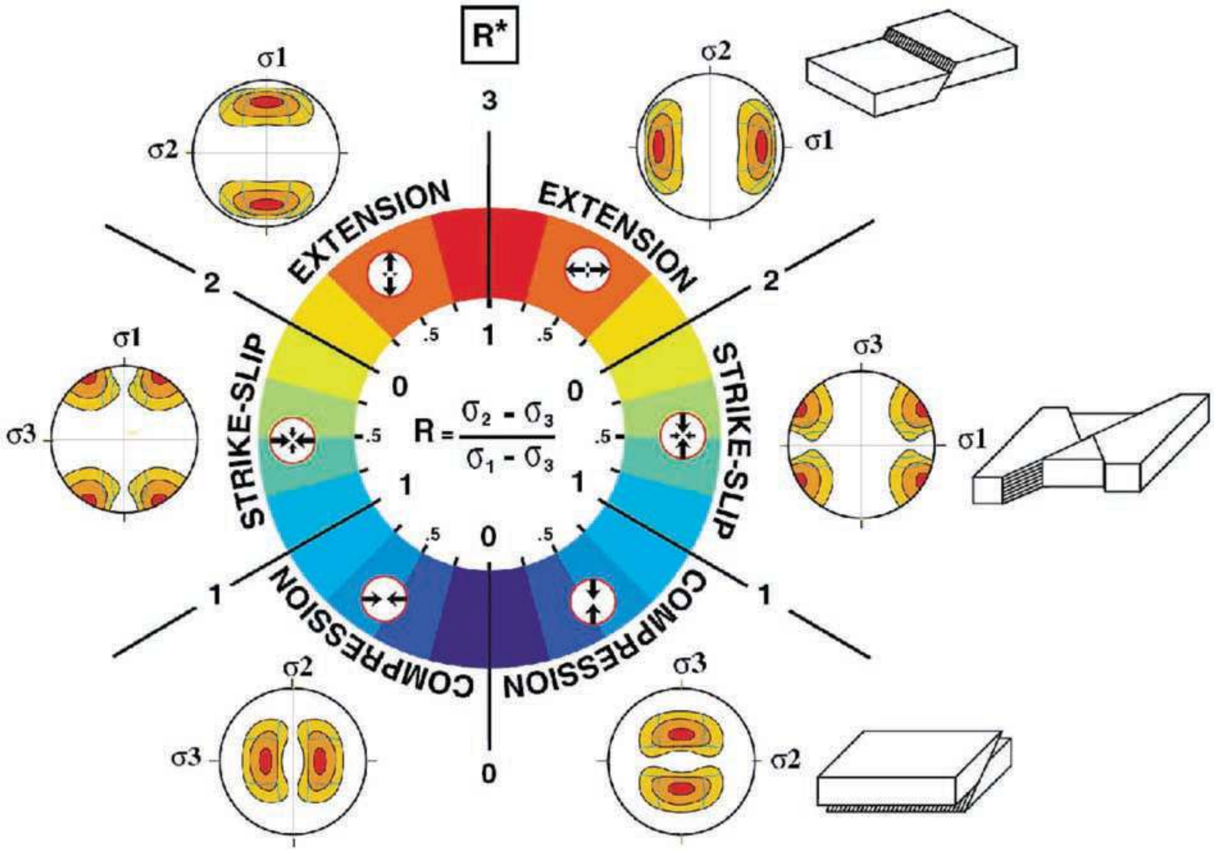

Figure 4. The relation between the stress shape factor *R* (varying from 0 to 1 in the inner circle) and the type of tectonic faulting. The *R** factor on the outer circle is a linear transformation of *R* so that *R** varies from 0 in compression to 3 in extension. The stereonet diagrams show the orientation of the principal stress axes and the contour plots of normals highlight the orientations where the fault verify the Mohr-Coulomb failure criterion (for a *R* of 0.5 and a friction angle of 25°). Note that the principal stresses are ranked following the continuum mechanics convention. (Modified from *Sassi and Faure* [1997] with permission from Elsevier.)

ate) are close, indicating a potential failure in reverse faults with a high dispersion in azimuth.

[25] Similar regions can be distinguished on the bottom view in Figure 7b. The bottom outer and inner arc have similar stress state and failure mode as the top outer and inner arc, respectively. There is thus a variation in stress state and failure mode through the thickness of the plate. For example, looking at the center of the fold (elements E6T and F5B), the principal stress directions are identical but the vertical stress is intermediate and minor at the top and bottom, respectively. At this central location, the failure modes is composed of axial joints and strike-slip (or normal) faults at the top and reverse faults striking E-W at the bottom.

[26] The elastic solution of folding is instrumental to explain qualitatively the potential first failure mode and its spatial variation over the structure. It could be applied to the laboratory experiments reported by *Withjack and Scheiner* [1982] for explaining the fault patterns in the Frontier sandstone reservoir of the Elk basin dome (Rocky Mountains). Our methodology would provide a better assessment of the stress histories prior to faulting. However, the stresses are not realistic during the fold development beyond the first potential activation. For example, we reproduce here part of the first fracture pattern discussed by *Gholipour* [1998] for the Oligo-Miocene Asmari carbonate reservoirs (Khuzistan, southwest Iran), but not its evolution during folding. The objective of sections 4–6 is to amend the rock rheology and to detect the activation of pervasive inherited discontinuities before and during folding.

4. Activation of Inherited Discontinuities

[27] This section explores the role of inherited discontinuities in the development of a fold. It is proposed that the studied structure is pervasively fractured prior to any deformation in up to two orientations and that the fracture activation is in a sliding mode only. Sections 4.1 and 4.2 are concerned with inherited systematic joints (vertical planes) and weak interlayers (horizontal planes), respectively. Section 5 will complement that analysis by including the possibility for new orientations to be activated.

4.1. Activation of Inherited Systematic Joints

[28] Systematic joints are represented by vertical surfaces with the second Euler angle set to either θ_2 = 40°

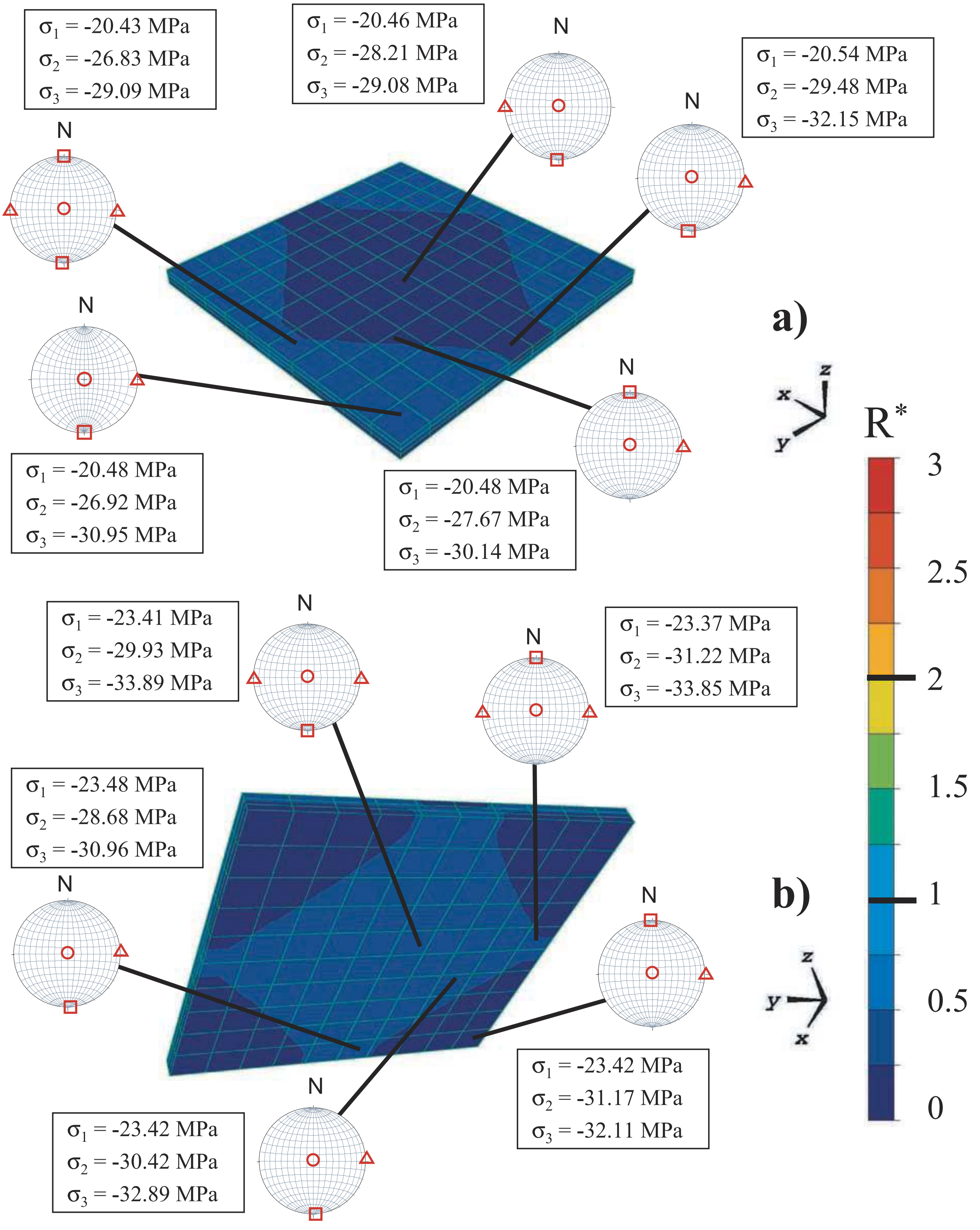

Figure 5. Isocontours (20) of the principal stress ratio over the elastically deformed structure prior to buckling (point P_1 in Figure 3). The stereonet diagrams provide the orientation of the principal stresses (circle, σ_1; triangle, σ_2; and square, σ_3) with the *x* axis oriented to the north.

(simulation 3) or θ_2 = 50° (simulation 4) and corresponding to a strike of N050° and N040°, respectively. The first and second Euler angles defining the orientation of the normal **n** are the angle between **n** and the vertical axis and the angle between the projection of **n** in the horizontal plane and the *x* direction, respectively (Figure 1b). Note that these sets of discontinuities strike obliquely with respect to the fold axis obtained with the elastic solution

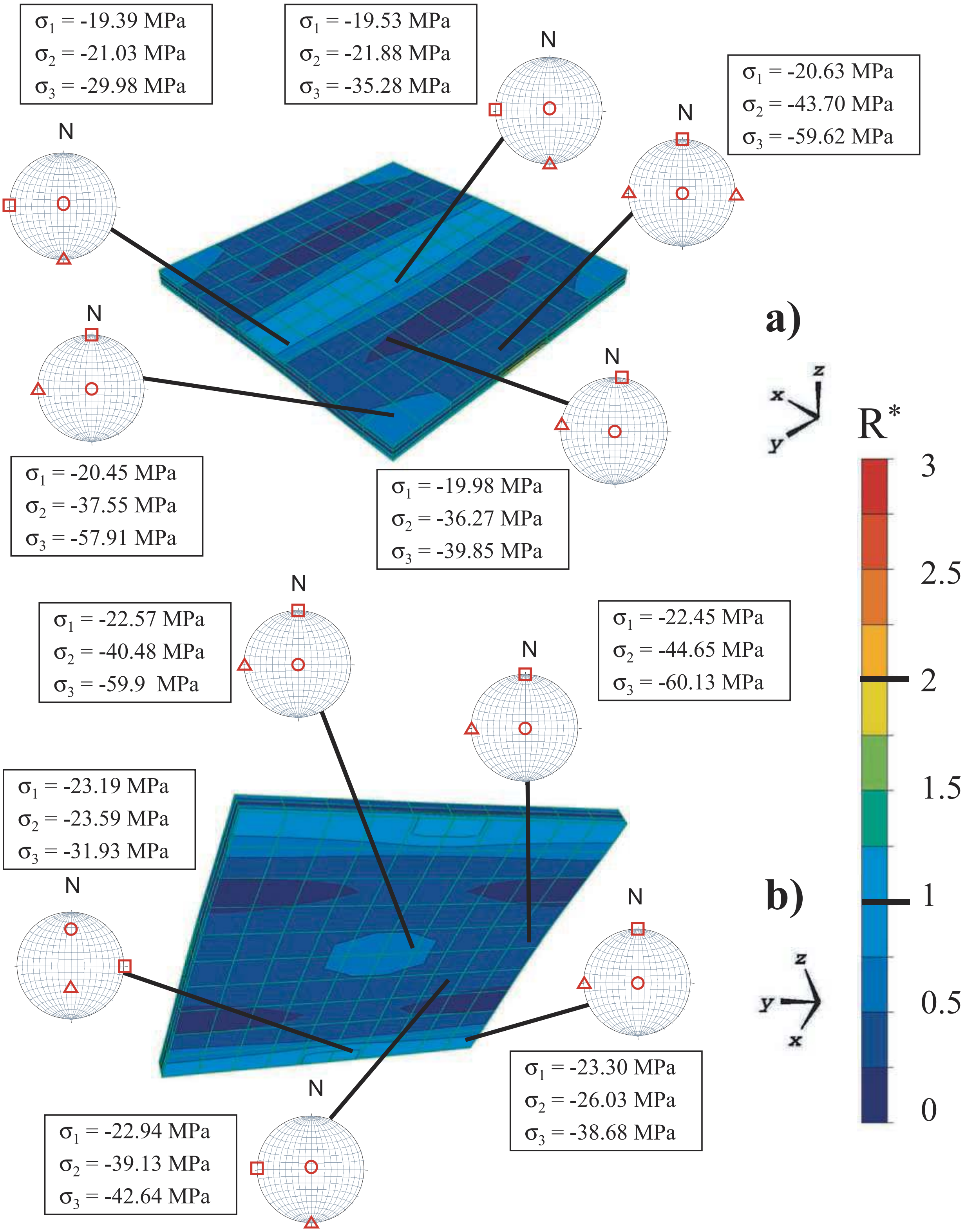

Figure 6. Isocontours (20) of the principal stress ratio over the elastically deformed structure during buckling (point P_2 in Figure 3). The stereonet diagrams provide the orientation of the principal stresses (circle, σ_1; triangle, σ_2; and square, σ_3) with the x axis oriented to the north.

reported in section 3. Evidences of the activation during folding of inherited systematic joints, striking obliquely with respect to a fold axis, are reported, for example, in the Frontier sandstone outcropping in the limb of the Split Mountain anticline (Utah) [*Silliphant et al.*, 2002]. For the simulations the cohesion, friction, and hardening in sliding mode of the joints are set to 20 MPa, 0.6, and 10 MPa, respectively.

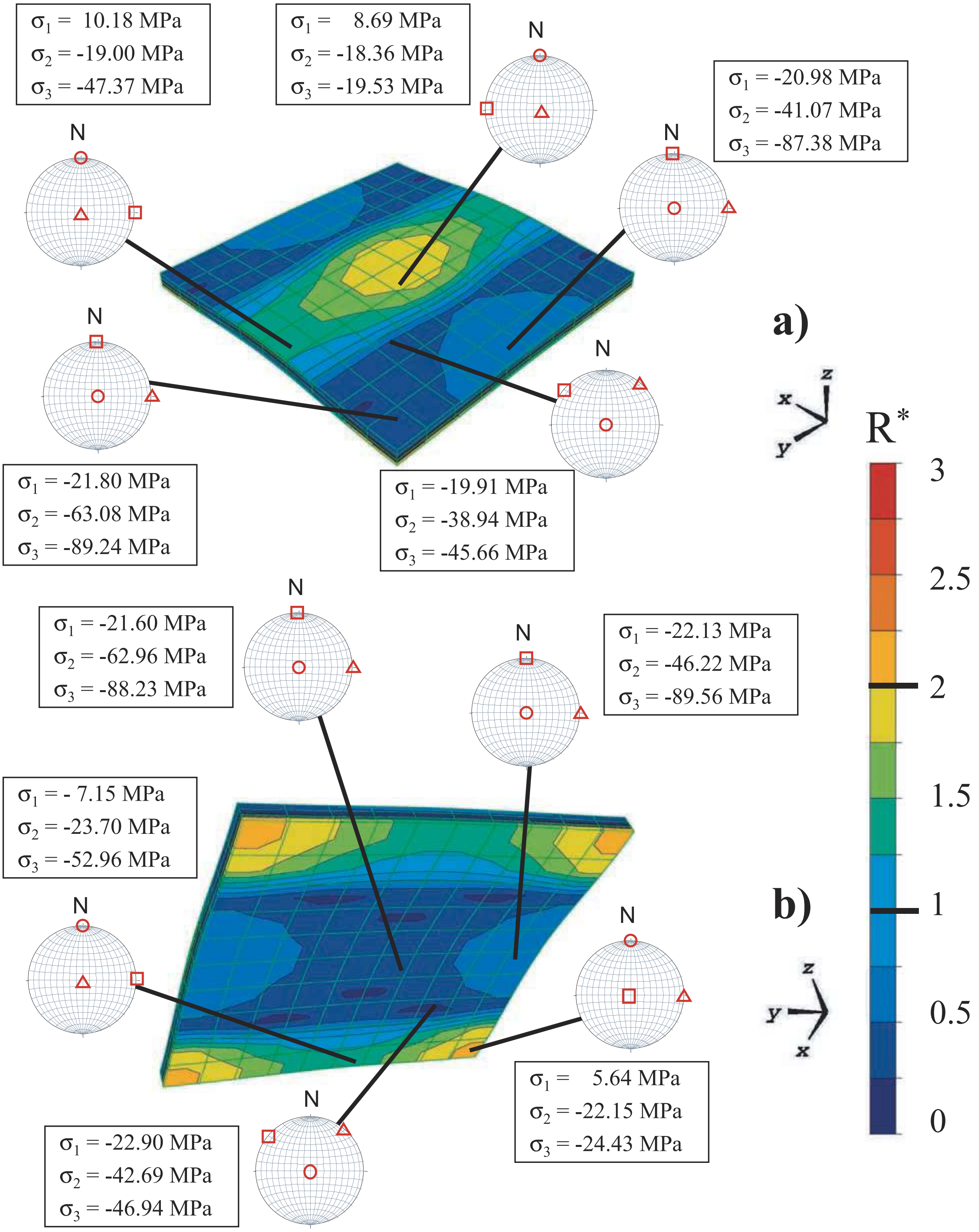

Figure 7. Isocontours (20) of the principal stress ratio over the elastically deformed structure during buckling (point P_3 in Figure 3). The stereonet diagrams provide the orientation of the principal stresses (circle, σ_1; triangle, σ_2; and square, σ_3) with the x axis oriented to the north.

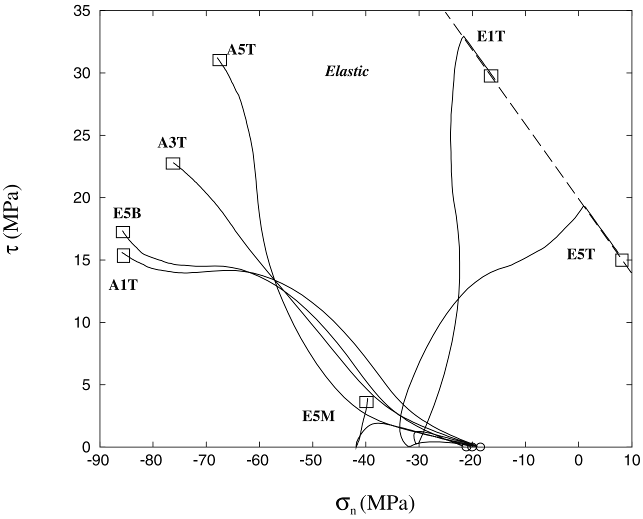

Figure 8. The time history of the resolved shear stress and the normal stress for vertical fractures striking N040° (simulation 4) at different locations in the fold identified by two letters and a number, a notation defined in Figure 2. The circles and the squares denote the initial and final stress states, respectively. The dashed segments mark the boundary of the initial elastic domain.

[29] The results of the two simulations in terms of $P\text{–}\delta$ curves correspond to curves 3 and 4 in Figure 3. There is no difference between the elastic solution (curve 2), and these two new simulations before the onset of buckling which is thus elastic. It is close to point P_3, in the postbuckling regime, that fractures are first activated. The set striking at N050° in simulation 3 is better oriented for activation than the set at N040° in simulation 4. This result is consistent with the elastic solution shown in Figure 7. The two $P\text{–}\delta$ curves of simulations 3 and 4 separate from the elastic solution with curve 4 keeping a positive slope. For simulation 3, there is a maximum load followed by a negative slope signaling a stability transition.

[30] The stress path during folding and the activation of the fractures are presented for simulation 4 in a space spanned by the resolved shear stress and the normal stress for the plane striking N040° in Figure 8. The circles and the squares represent the initial and final stress states, respectively. The elastic domain is delimited by a dashed line defining the initial Mohr-Coulomb criterion for the inherited set. There are three circles because the normal stress is depth-dependent in the initial configuration. The resolved shear stress is of course zero initially because the two horizontal principal stresses are first identical. The curves in Figure 8 are obtained at various positions within the structure and they can be arranged in three groups. The four curves close to the one obtained for element A3T are from the inner arc either on the top or the bottom layers of elements and constitute the first group. Note that elements are identified as before even though the number of elements (9 × 9) requires a different range for the letters and integers (A to I and 1 to 9 only). The normal stress is large, and the resolved shear stress is not sufficient to trigger fault activation. The second group is composed of the single curve E5M found at middle depth at the structure center. The stress evolution is minor compared to the first group. The last group is the most interesting and is composed of the stress paths for elements E1T and E5T found in the outer arc. The normal and resolved shear stresses are increasing during the elastic buckling until fractures in E5T are first activated. Beyond that first activation, followed by the activation in E1T, the resolved shear stress decreases along the direction set by the Mohr-Coulomb line. There is thus a tendency for the stress to evolve toward tensile normal stresses which should trigger an opening of fractures (see element E5T). Looking at the elastic solution (Figure 7), the activation in these elements was predicted: a failure mode in strike-slip was foreseen in view of the stress shape factor larger than 1.

[31] The results discussed above could be compared to the observations of *Silliphant et al.* [2002], despite the difference in depth and folding mode (forced versus buckled fold). We predict the observed activation of the inherited systematic joints in the fold closure area (for example, position E1T). It is suggested that this activation occurred also at the top of the fold which is eroded.

4.2. Activation of Interlayer Slips and Systematic Joints

[32] Simulation 5 is the last reported in this section and concerns the vertical inherited set of simulation 4 striking at N040° plus a horizontal set which mimics the weakness of bedding interfaces. The cohesion, friction coefficient, and hardening modulus are set to 0, 0.1, and 10 MPa, respectively, for this horizontal set. The friction coefficient along the bedding planes has to be lower than 0.2 to ensure that this orientation is activated. This activation is rather unstable numerically and a viscoplasticity extension of the model presented in section 2 is employed for the two orientations. The linear viscosity function presented in Appendix B is selected, and the viscosity constant is set to 10^{19} Pa s for a nominal strain rate of 10^{-12} s^{-1}. The $P\text{–}\delta$ curve of this simulation is curve 5 in Figure 3. This curve is close to the elastic solution because of the viscosity effects during buckling. This result illustrates how time-dependent rheology could delay the stability transition (or the maximum load), compared to the strain-rate-independent results obtained for simulation 4 (or 3). Of more interest here is the activation of the two families of inherited discontinuities which are analyzed with the help of Figure 9. Figure 9a for the bedding planes shows that the evolution of the normal stress and of the resolved shear stress occurs over a small range compared to the one found in simulation 4. The normal stress is always of the order of −20 MPa and the resolved shear stress is less than 10 MPa. There are three groups of curves in Figure 9a corresponding to three initial stress states encountered at the top, middle, and bottom layer of the structure. The evolution is similar for the top and bottom layers. It is in the middle of the structure that the resolved shear stress is more important and where sliding first occurs during the initiation of buckling. The bedding sliding occurs first in the fold limbs (e.g., elements C3M, C8M, H3M, and H8M) and then spreads over the whole mid region and in the fold limbs at the top and bottom of the structure. The distance between the final stress state and the yield surface is of the order of 5 MPa and the strain rate of the

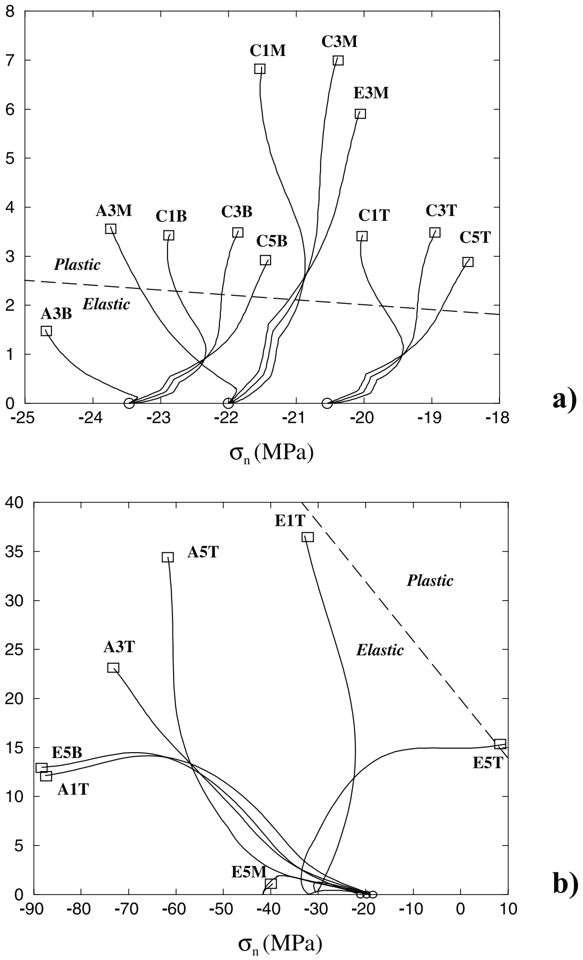

Figure 9. The time histories (simulation 5) of the resolved shear stress and the normal stress (a) for inherited horizontal discontinuities and (b) for vertical fractures striking N040°, at different locations in the fold. The circles and the squares denote the initial and final stress states, respectively. The dashed segments mark the boundary of the initial elastic domain.

order of 5 10^{-12} s^{-1}, which is 5 times the nominal strain rate.

[33] The influence of the sliding over the bedding planes on the activation of the set of vertical joints which have been considered here is now discussed. From Figure 9b, it is observed that the evolution of the stress state on these vertical joints is qualitatively similar to the one observed without sliding along bedding planes (see Figure 8), but the activation is now reduced. This result is in line with the finding of the experiments reported by *Couples and Lewis* [2000]. Also, the model problem presented here could be seen as a 3-D generalization of the 2-D analysis of *Cooke et al.* [2000] proposed to explain the interlayer slips in the Navajo aeolian sandstone outcropping in the limb of the East Kaibab monocline (Utah). The role of weak bedding planes is not explored further in the rest of this paper because of the similarity of the stress histories, with or without interlayer slips.

[34] A single vertical orientation was considered in this section. It has been shown that the normal stress evolves toward the tensile domain because of the buckling kinematics. There are thus reasons for investigating the activation of other orientations and to include also the activation in an opening mode. These two objectives are considered in section 5.

5. Synfolding Fracture Pattern

[35] A continuous description of the fracture orientation is not possible and a distribution every 10° for the two Euler angles is instead proposed. Every orientation lumps the contribution of fractures in its neighborhood. This lumping should be accounted for by a numerical factor or integration weight. This factor is combined here directly with the material properties of the orientations. To differentiate between new and inherited fractures, the former are assumed to have larger cohesion, tensile strength and hardening moduli. Consequently, the four parameters c_{S0}, c_{S1}, c_{O0}, and c_{O1} of the plasticity model are assigned values 5, 10, 5, and 10 MPa for the inherited fractures and 40, 100, 8, and 100 MPa for the new fractures. A friction coefficient of 0.6 is considered for all orientations.

[36] Two simulations are documented here and they differ by the orientation of the inherited fractures. In simulation 6, there is a single set of vertical discontinuities striking N040° as in simulation 4. In simulation 7, the inherited set is also vertical but striking E-W. This particular choice is proposed to investigate the influence of discontinuities created during an early compressive stage prior to buckling. The typical example in the field would be stylolites which are compressive features perpendicular to the principal compressive directions often activated in opening during folding.

5.1. Activation of Inherited Joints and of New Fractures

[37] The presence of inherited discontinuities is often not sufficient to accommodate the final deformation due to folding. This is the case, for example, in the Frontier sandstone reservoir of the Oil Mountain anticline (Wyoming) reported by *Hennings et al.* [2000]. To study this possibility, the opening and sliding of new discontinuities, together with the activation of inherited joints, are permitted in the simulation 6, which is now discussed.

[38] The $P-\delta$ curve for simulation 6 is presented as curve 6 in Figure 3. The stress histories for this simulation is found in Figures 10a and 10b for the inherited set and for a new vertical fracture set striking N100°, respectively. The activation of the fractures occurs in the postbifurcation range for a load larger than the Euler load between the load levels P_2 and P_3. This activation occurs on the inherited set before the load level achieved in simulation 4 because the cohesion is now smaller. However, the two stress histories are rather similar, as one can see by comparing Figures 10a and 8. The activation of the inherited set perturbs the local stress state and influences the opening of new vertical fractures in the outer arc, as predicted by the elastic solution. However, the new orientation corresponds to vertical joints striking N100° instead of the N090° expected by the elastic solution. The stress history on that N100° plane is found in Figure 10b and share some similarities with Figure 10a. The main difference could be described by a scaling of the two axis: the resolved shear stress increase

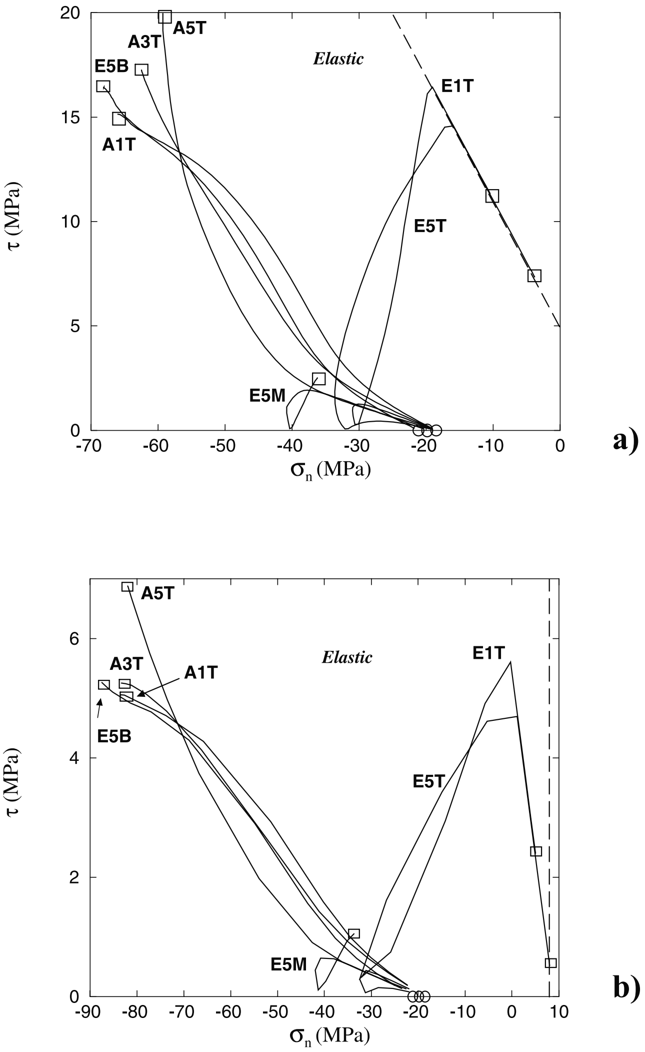

Figure 10. The time histories (simulation 6) of the resolved shear stress and the normal stress (a) for inherited vertical fractures striking N040° and (b) for new vertical fractures striking N100°. The circles and the squares denote the initial and final stress states, respectively. The dashed segments mark the boundary of the initial elastic domain.

is minor whereas the normal stress changes more drastically. The elements in the inner arc are sustaining a compression and cannot open. It is in the outer arc that elements such as E1T to E5T are activated in an opening mode. This activation occurs first in the fold center and spreads along the outer arc axis. Note that the resolved shear stress trajectories is modified before the opening (sharp decrease in τ), as a result of the activation of the inherited set. The $\tau - \sigma_n$ curve follows a straight segment toward the opening cutoff which is dictated by the evolution of the resolved shear stress along the Mohr-Coulomb line of the inherited set. This strong interaction is simply due to the assumption that the same macrostress acts on the two fracture sets. The joint set opening in the outer arc has a drastic consequence on the load bearing capacity of the structure, curve 6 in Figure 3. At the end of the simulation, the displacement at the boundary is nearly constant in time while the load drops sharply. This response is characteristic of the development of an instability: the nominal strain rate tends to zero, whereas the local strain rate in the fold outer arc is increased by several orders of magnitude. As a final remark, note that the activation of the new outer arc joints leads to a reduction of the stress magnitude in the outer arc and, consequently, eliminates any opening of the inherited set which was foreseen in simulation 4. This is a second strong interaction between inherited and new fractures.

5.2. Activation of "Stylolites" and of New Fractures

[39] The second simulation of this section (simulation 7) proposes a simple interpretation for the inherited set. This set is vertical and perpendicular to the major compressive direction and is seen as composed of stylolites which are formed during the early compression prior to buckling as suggested, for example, by *Averbuch et al.* [1992] for the Cenozoic cover of Lagrasse fold in the northeastern foreland of Pyrenees. Also, for the Devonian sandstone folded in the Tata province (Moroccan Anti-Atlas), large compressive stresses of the order of 100 MPa were predicted numerically by *Guiton et al.* [2003] during the early compression phase prior to buckling. Stylolites have been reported in the same area by *Cortes* [2000]. The details of the compaction mechanism responsible for the stylolites are not considered here nor the associated loss of mass. The stylolites constitute a weak orientation which could be activated either in opening or sliding during buckling. New orientations are also considered as in section 5.1 (simulation 6).

[40] It is found that during folding, the inherited set is the only system which is activated. The P–δ curve of this simulation is curve 7 in Figure 3. Figure 11 presents the stress history for the inherited set of stylolites at the element E5T. Only the normal stress is represented, as a function of the normalized displacement at the boundary, since the resolved shear stress remains close to zero at all times. The activation of the inherited set occurs in the postbuckling range between load P_2 and load P_3. This activation occurs first at the top center of the structure (element E5T) under increasing load but, as the activation spreads to the whole outer arc, the load bearing capacity drops drastically.

[41] A similar chronology is reported in the Precambrian quartzite of the Baraboo syncline (Wisconsin) by *Dalziel and Stirewalt* [1975]. They suggest, first, the formation of planes of dissolution perpendicular to the major compressive direction during the early layer-parallel shortening and, second, the opening reactivation of these planes because of the outer arc extension associated to the folding.

6. Prefolding Fracture Pattern

[42] All the discontinuities studied so far are activated during the buckling development. This section accounts for fracture activation prior to buckling. This early deformation is homogeneously distributed over the structure. For example, *McQuillan* [1973] suggests that the carbonate of the Asmari reservoir, in several anticlines of the Zagros mountain foothills, was pervasively fractured in many orientations before folding. These sets of discontinuities constitute preferential sites for further sliding or opening or, to the contrary, could be deactivated during folding in certain regions of the structure. To investigate this scenario, the

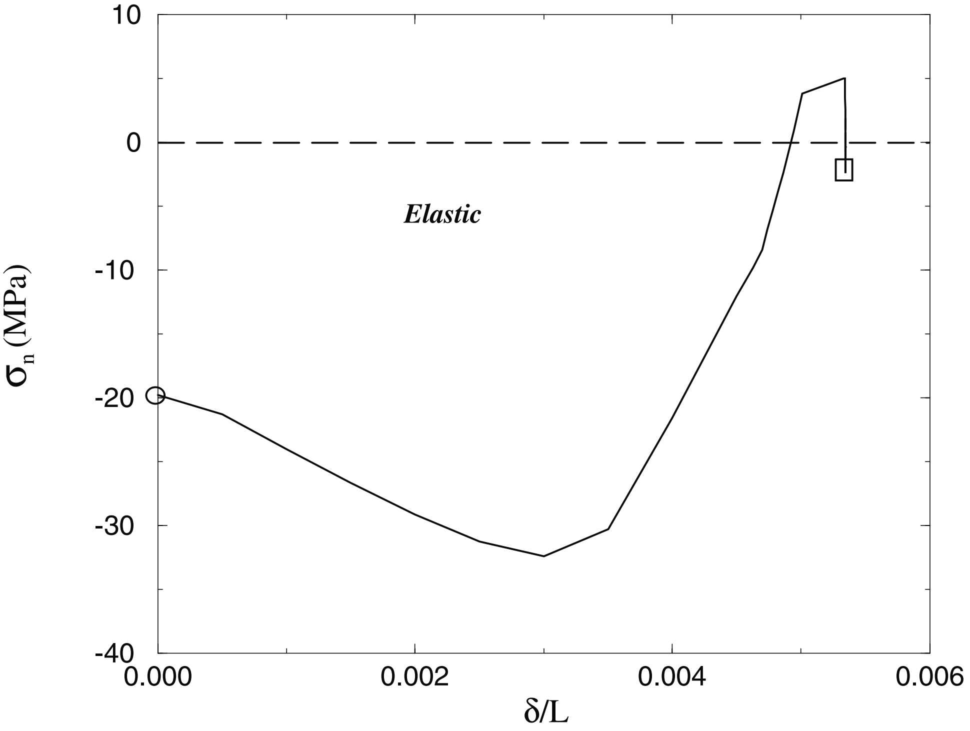

Figure 11. The time histories (simulation 7) at the top center of the structure of the normal stress on inherited planes striking N090° and the prescribed displacement at the boundary. The circle and the square denote the initial and final stress states, respectively. The dashed line marks the boundary of the initial elastic domain.

last simulation reported here assumes that all orientations are potentially activated with a discretization of the hemisphere by 10°, for the two Euler angles. The same material properties are considered in all orientations. The friction coefficient is set to 0.3 and the cohesion and tensile strength to 0 and 5 MPa, respectively. The hardening moduli for sliding and opening take for values 100 MPa. A viscosity of 10^{19} Pa s for a nominal compression rate of 10^{-12} s^{-1} complement the data set.

[43] The $P–\delta$ curve 8 in Figure 3 results from this simulation. Buckling is marked by a maximum load at 90% of the Euler load, and is followed by the characteristic structural softening observed for the previous simulations. It should be noted that buckling is initiated at a load and displacement which are close to the elastic solution, curve 2. Activation of discontinuities has not yet resulted in a noticeable accumulation of irreversible macrodeformation. However, this activation has already reduced the apparent stiffness of the structure which determines the plastic buckling load (see *Leroy and Triantafyllidis* [1996] for further discussion).

[44] The discontinuities first activated prior to buckling are conjugate reverse faults striking E-W (Figure 12a), as predicted by the elastic solution. This information is read from the stereonets presenting isocontours of the poles to the activated orientation, weighted by the associated internal variables for sliding γ or for opening d. The contours are normalized by the maximum magnitude of the internal variable which is written next to every stereonet with a normalization by a factor of 10^{-4}. The color code is white to black for an intensity varying from 0 to 1. The amount of irreversible deformation is small (Figure 12a), confirming the interpretation made from the $P–\delta$ curve. Sliding occurs first at the north and south plate boundaries and then takes place over the whole structure through its thickness before buckling initiates.

[45] The first phase of buckling (Figure 12b) is characterized by the rather elliptical mode reported above at the end of the previous simulations. The fracture activation in the limb (element H4T) is not modified by buckling. It is not the case at the saddle point (element I5T) where more vertical orientations are now activated in a compressive mode. This evolution from the early reverse faults toward conjugate strike-slip faults is consistent with the stress shape factor for the elastic solution (Figure 7a) close to 0.6. On the fold outer arc (elements E1T and E5T), activated conjugate faults are dipping subvertically to nearly 30°. The planes dipping around 30° and striking about E-W correspond to the reverse faults discussed above and the subvertical faults suggest strike-slip to extensive regime. This interpretation is consistent again with the elastic solution in Figure 7a, where the stress shape factor ranges from 0 to 2.25. Opening was however not observed at that stage of loading because of the zero cohesion adopted for all orientations.

[46] The development of the fold is marked by a change in geometry from elliptical to circular during the loss of bearing capacity of the structure (Figure 3). This change in kinematics was not observed before and is thus due to the ease of activating numerous discontinuities. The change in mode results in a local rotation of the principal stress directions and the deactivation of various orientations. To document this effect, two stereonets are plotted from the

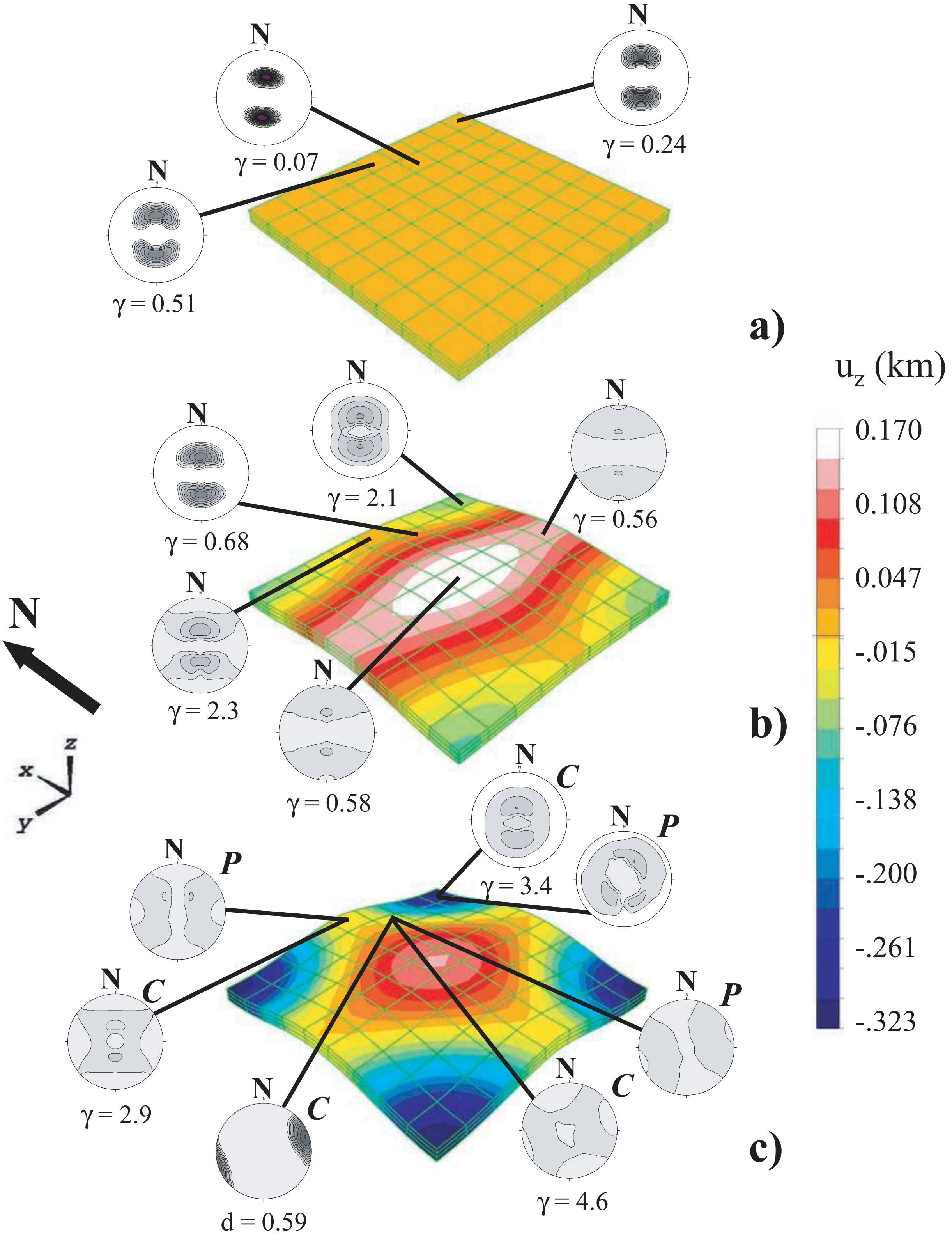

Figure 12. Isocontours (20) of the vertical displacement (km) over the structure at three stages of simulation 8. The isocontours are plotted (a) prior to buckling, (b) during the first buckling phase in an elliptical mode, and (c) at the end of the simulation after the switch to the circular mode. The stereonet diagrams (Schmidt projections on the lower hemisphere) show iscontours of the activated poles weighted by the macro permanent deformation. Each plot is normalized by the maximum value at the site which is also indicated next to the stereonet with a normalization by a factor of 10^{-4}. The γ and *d* identify the mode of activation in sliding or opening, respectively. In Figure 12c, the P and C differentiate between present and cumulated activation.

same locality, marked by C and P which stand for cumulated activation and presently activated, respectively. The fracture pattern is not yet modified in the outer arc regions from elements E1T to E5T. The saddle point of Figure 12b, element I5T, is now an outer arc for a fold having the *x* direction for axis. At this site, the activated fracture pattern is in strike-slip mode. In the fold limb, element H4T, there is a rotation of the principal stress directions which is marked by the activation of strike-slip conjugate faults, anticlockwise rotated with respect to the pattern found in element I5T. Note that joints striking NNW-SSE are now activated at the same locality. This is the only place on the fold where discontinuities are found to be open. In the inner arc regions, the four corners of the plate, the presently activated pattern shows a clockwise rotation compared to the C stereonet and a deactivation of the subhorizontal planes. This newly activated fracture pattern corresponds to reverse faults striking NW-SE.

7. Concluding Discussion

[47] An elastoplasticity model, which accounts for the presence of diffuse inherited weak directions or of new orientations dictated by the local stress state, is applied to analyze quantitatively the relation between buckling in three dimensions and fracture pattern activation.

[48] The principal stress directions and magnitudes predicted with an elasticity theory provide the critical orientation and mode of potential faulting, with the application of a Mohr-Coulomb criterion and the analysis of the stress shape factor. Potential joints could also be inferred from the elastic solution if a tensile stress is detected. Folding occurs in three stages, and the failure modes inferred from the elastic solution are as follows. During stage 1, prior to buckling, the deformation is approximately homogeneous with potential reverse faulting. Stage 2 is characterized by the initiation of buckling in a cylindrical mode, with an increase in compression in the inner arc which could lead to reverse faulting and to strike-slip faulting in the emerging outer arc. During stage 3, the development of the three-dimensional ellipsoidal fold leads to tensile principal stress in the outer arc, where strike-slip to normal faults as well as joints could be expected. This elastic solution, however, cannot describe the relation between the fracture activation and the three stages of fold development, common to most of the simulations reported.

[49] This interaction has been studied starting with inherited discontinuities perpendicular to the bedding and chosen not to be parallel to the minor and major axes of the fold. Buckling is elastic, but the diffuse discontinuities are sliding in the outer arc during the fold development. The activation of bed-perpendicular discontinuities is found to be delayed and reduced in the presence of sliding along bed-parallel discontinuities, representing weak bedding interfaces. The stress path in a space spanned by the normal stress and the resolved shear stress for the vertical weak orientation is pointing toward the tensile domain during the final stage of buckling, suggesting the possibility that discontinuities could open. When this possibility is accounted for, new joints striking at an angle to the fold axis are found to open. This orientation, not predicted by the elastic solution, is due to the rotation of the principal stress directions during the earlier sliding along the inherited vertical discontinuities. Furthermore, opening of the new orientations limits the evolution of the normal stress toward tensile values for the inherited vertical discontinuities which remain closed. This opening of discontinuities reduces drastically the structure bearing capacity: the final stage of buckling is governed by a redistribution of the elastic stored energy without any further displacement at the boundaries.

[50] It should be noted that during the early compression prior to folding, the compressive stresses could be responsible for a compaction by pressure solution, resulting in stylolitic surfaces, which has not been modeled here. These surfaces define a weak orientation if the normal stress becomes tensile during buckling. To explore that possibility, a weak orientation parallel to the fold axis has been introduced and shown to be open during stage 2 of fold development in the outer arc.

[51] Finally, the response of poorly consolidated sediments is explored. It is characterized by a layer-parallel shortening, defined here as the homogenous compressive deformation during stage 1, accommodated in a reverse fault mode. This early activation reduces the buckling load compared to the elastic Euler load. The ellipsoidal mode of folding is accommodated by strike-slip faulting in the fold limbs and strike-slip to normal faulting in the outer arc. Furthermore, folding evolves from the ellipsoidal mode toward a circular collapse mode. Reverse faulting is then deactivated in the limbs and is replaced by both strike-slip faulting and opening of joints, oriented consistently with the circular shape of the fold.

[52] The application presented here of the elastoplasticity model of *Leroy and Sassi* [2000] should be seen as an attempt to reproduce in a simple manner the activation of discontinuities in both sliding and opening. The reported complexity of the fold structural evolution in the presence of inherited weak orientations confirms the necessity to apply first such simple models to palliate to the limitations of the elastic solution. Furthermore, it was shown that there is a connection between the rheological parameters of the plasticity model and the density and size of fractures, represented as penny-shaped cracks in an otherwise elastic matrix. Further work is required to strengthen this link. For example, the last results presented in this paper were in the form of distributions in stereonet diagrams of the two internal variables for the activated orientations: the macro irreversible deformation in shear and dilation. These two variables could be seen as the first estimates of the sums of the sliding and opening of every discontinuity sharing the same orientation in the representative volume element. These two internal variables should be linked in the future in a more concrete way to the density and size of the fractures. The study of exhumed structures should provide the statistical distribution between the fracture geometrical characteristics and the overall accommodated deformation [*Rives et al.*, 1992]. A qualitative attempt, which was found useful to constrain the fracture activation chronology, is given by *Guiton et al.* [2003]. Field data should provide the basis for calibrating quantitatively the next plasticity models in order to obtain a predictive model for subsurface structures of

similar formations. It is hoped that the predictions for naturally fractured reservoirs could then be instrumental in constructing their subseismic fracture networks.

Appendix A: Kinematics and Weak Formulation of Equilibrium

[53] The objective of this appendix is to introduce the principle of virtual power which is at the basis of the finite element approximation. Further information on the numerical scheme are given by *Guiton* [2001].

[54] The Green-Lagrange deformation tensor

$$\mathbf{E} = \frac{1}{2}(\nabla\mathbf{u} + {}^t\nabla\mathbf{u} + {}^t\nabla\mathbf{u}\cdot\nabla\mathbf{u}), \tag{A1}$$

in which $\mathbf{u}$ and ∇ are the displacement field and the gradient operator, is the necessary strain tensor in the presence of finite rotations encountered during folding. The weak formulation of equilibrium is the principle of virtual power

$$\int_{\Omega_0} \boldsymbol{\tau} : \tilde{\mathbf{e}} dV = \int_{\partial\Omega} \tilde{\mathbf{v}}.\mathbf{T} dS + \int_{\Omega_0} \rho_0 \mathbf{b}\cdot\tilde{\mathbf{v}} dV, \tag{A2}$$

where $\boldsymbol{\tau}$, $\tilde{\mathbf{e}}$, $\tilde{\mathbf{v}}$, $\mathbf{T}$, ρ_0, and $\mathbf{b}$ are the second Piola-Kirchhoff stress tensor, the virtual lagrangian strain rate tensor, the virtual velocity, the prescribed force per unit area on part of the boundary in its current configuration $\partial\Omega$, the material volumetric mass in the reference configuration Ω_0 and the body force acting on the solid, respectively. The virtual Lagrangian strain rate tensor and the virtual velocity are related by

$$\tilde{\mathbf{e}} = \frac{1}{2}(\nabla\tilde{\mathbf{v}} + {}^t\nabla\tilde{\mathbf{v}} + {}^t\nabla\tilde{\mathbf{v}}\cdot\nabla\mathbf{v} + {}^t\nabla\mathbf{v}\cdot\nabla\tilde{\mathbf{v}}). \tag{A3}$$

[55] The force density $\mathbf{T}$ in this paper results from the action of the overburden and the substratum on the top and bottom surfaces of the domain, respectively. It is assumed that this action results in compressive forces directed along the current outward normal to the boundary, with an intensity proportional to the lithostatic pressure:

$$\mathbf{T} = -\rho_0 g(h_{\mathrm{Ref}} + z)\mathbf{n}, \tag{A4}$$

in which g, h_{Ref} and z are the acceleration of gravity, the initial middle depth of the studied domain and the current vertical position from this reference depth to the point of interest on the boundary. The transformation of the integral over the current position of the boundary in the right-hand side of equation (A2) to an integration over the reference configuration respecting the kinematic assumptions of small strain and finite rotation is given by *Guiton* [2001]. Note that the same volumetric mass is considered for the overburden material and the studied domain.

Appendix B: Numerical Algorithm

[56] This appendix pertains to the numerical algorithm for the elastoplasticity constitutive relations presented in section 2, which relies on the assumptions of small strain and finite rotation. Consider known at time t_n the macrostress τ^n and strain $\mathbf{E}^n$ as well as the internal variables γ_α^n and d_α^n which characterize the sliding and opening of a plane of discontinuity α oriented by its normal $\mathbf{n}_\alpha$. There are M such potential planes which correspond to either inherited weak directions or to new orientations of discontinuities. The finite number in the case of new fractures results from a discretization of the hemisphere. To simplify the notation, the list of $2M$ internal variables ξ_β is introduced to combine in a single notation the sliding and the opening modes. At time t_{n+1}, the finite element solution provides a series of estimates for the displacement increment resulting in the strain $\mathbf{E}^{n+1}$. The objective of this appendix is to determine the corresponding stress and the internal variables ξ_β^{n+1}. It requires the choice of an update algorithm, selected here to be fully implicit. Note that above and in what follows, the superscripts n and $n + 1$ determine if the quantity highlighted is estimated at time n or $n + 1$, respectively.

[57] The stress increment, defined as the difference between the macrostress at time $n + 1$ and n is

$$\Delta\boldsymbol{\tau} = \boldsymbol{\tau}^{n+1} - \tau^n = \mathbf{D}^e : \left. \quad \Delta\mathbf{E} - \sum_\beta^{2M} \Delta\xi_\beta \mathbf{R}_\beta^{n+1} \right), \tag{B1}$$

for a population of M orientations activated in either or both sliding and opening. The fourth-order tensor $\mathbf{D}^e$ in equation (B1) is simply, in the case of an isotropic elastic solid,

$$\mathbf{D}^e = \left(K - \frac{2G}{3}\right)\boldsymbol{\delta}\otimes\boldsymbol{\delta} + 2G\mathrm{I}_S, \tag{B2}$$

in which I_S, K, and G are the symmetric fourth-order identity tensor, which associates to any second-order tensor $\mathbf{A}$ the tensor $(\mathbf{A} + {}^t\mathbf{A})/2$, and the moduli of elasticity for bulk and shear deformation, respectively. In equation (B1), the tensor $\mathbf{R}_\beta^{n+1}$ represents the flow direction in stress space which is

$$\begin{aligned} \mathbf{R}_\beta^{n+1} &= \mathbf{R}_{S\beta}^{n+1} \equiv \frac{1}{2}\left(\mathbf{m}_\beta^{n+1}\otimes\mathbf{n}_\beta + \mathbf{n}_\beta\otimes\mathbf{m}_\beta^{n+1}\right), \\ \mathbf{R}_\beta^{n+1} &= \mathbf{R}_{O\beta}^{n+1} \equiv \mathbf{n}_\beta\otimes\mathbf{n}_\beta, \end{aligned} \tag{B3}$$

for either sliding (S) or opening (O). Note that the flow direction is determined at time t_{n+1} rendering the update algorithm equations (B1)–(B3) implicit in stress. This difficulty is only true for the sliding mode since the normal to the plane of discontinuity is oriented in the reference configuration and is thus independent of the deformation and of the stress path.

[58] The update algorithm is decomposed into a predictor and a corrector step. The predictor is constructed with the assumption that the increment in strain does not generate any irreversible deformation. The stress predictor denoted $\boldsymbol{\tau}^*$ is thus based on the elastic response and the internal variables take the values found at time t_n, $\xi_\alpha^* = \xi_\alpha^n$. These assumptions are combined with equations (B1) and (B2) to provide

$$\boldsymbol{\tau}^* = \boldsymbol{\tau}^n + \left(K - \frac{2G}{3}\right)\boldsymbol{\delta}\mathrm{tr}(\Delta\mathbf{E}) + 2G\Delta\mathbf{E}. \tag{B4}$$

[59] The validity of the assumptions postulated for the predictor step is now checked by inserting the estimates in

stress and internal variable in the $2M$ yield criteria (two for each orientation). If all yield conditions are satisfied, the predictor defines correctly the stress at the end of the time step. If there is a yield criterion found to be unsatisfied, a correction is required to account for the irreversible deformation. Let us assume that m yield conditions need to be enforced. The correction step then consists of solving the following set of (m + 6) equations:

$$\boldsymbol{\tau}^{n+1} = \boldsymbol{\tau}^{*} - \sum\nolimits_{\beta}^{m} \Delta\xi_{\beta} \cdot \left(\left(K - \frac{2G}{3} \right) \boldsymbol{\delta}_{\beta O}\, \delta + 2G\mathbf{R}_{\beta}^{n+1} \right),$$

$$\phi_{\beta}\left(\boldsymbol{\tau}_{\beta}^{n+1}, \xi_{\beta}^{n+1}\right) = 0 \qquad (\beta = 1, .., m), \tag{B5}$$

in which the Kronecker $\delta_{\beta O}$ is zero or one if β corresponds to an internal variable for sliding or for opening, respectively. This symbol marks the fact that the flow direction $\mathbf{R}_{\beta}^{n+1}$ has a zero trace in sliding and a trace of one in opening. The m equations in the second line of equation (B5) correspond to the yield conditions which are enforced at the end of the time step in this implicit algorithm. The exact expressions of the yield criteria are presented in section 2.

[60] Some of the simulations reported in this paper are based on the extension to viscoplasticity of the present model. There is of course a physical justification for introducing a strain rate dependency but it was done here mainly for sake of numerical stability. It is a linear overstress model which is considered and the new algorithm is obtained by replacing the m equations in equation (B5) by the viscosity functions:

$$\Delta\xi_{\beta} = \frac{\Delta t}{\eta} \phi_{\beta}\left(\boldsymbol{\tau}_{\beta}^{n+1}, \xi_{\beta}^{n+1}\right) \quad (\beta = 1, .., m), \tag{B6}$$

in which η is the viscosity parameter. Note that ϕ_{β} is then a loading surface in stress space and not the boundary of the elastic domain as for time-independent plasticity.

[61] The update algorithm has been completely defined for both strain- rate-dependent and strain-rate-independent cases. The linearization of these algorithms, to obtain the consistent tangent required for the Newton-Raphson algorithm [*Simo and Taylor*, 1985], is not presented here for sake of conciseness and is given by *Guiton* [2001].

[62] **Acknowledgments.** This work is part of the first author's Doctorate thesis which was supported by the Institut Français du Pétrole (Division of Geology and Geochemistry) and TotalFinaElf (Exploration and Production). This support is gratefully acknowledged. D. Frizon de Lamotte (Université de Cergy-Pontoise) and J. P. Petit (Université de Montpellier) suggested study of the role of stylolites and of weak bedding interfaces, and they are thanked for their continuous encouragements. J. Urai (University of Aachen, Germany) and an anonymous reviewer are also thanked for their critical remarks that helped to write the final version of this paper.

References

Averbuch, O., D. Frizon de Lamotte, and C. Kissel, Magnetic fabric as a structural indicator of the deformation path within a fold-thrust structure: A test case from the Corbières (NE Pyrenees, France), *J. Struct. Geol.*, *14*(4), 461–474, 1992.

Batdorf, S. B., and B. Budiansky, A mathematical theory of plasticity based on the concept of slip, *U. S. NACA Tech. Note*, *1871*, 1949.

Biot, M. A., *Mechanics of Incremental Deformations*, John Wiley, New York, 1965.

Bott, M. H. P., The mechanics of oblique slip faulting, *Geol. Mag.*, *96*, 109–117, 1959.

Budiansky, B., and R. J. O'Connell, Elastic moduli of a cracked solid, *Int. J. Solids Struct.*, *12*, 81–97, 1976.

Bui, H. D., *Mécanique de la Rupture Fragile*, Masson, Paris, 1978.

Carter, N. L., and M. C. Tsenn, Flow properties of continental lithosphere, *Tectonophysics*, *136*, 27–63, 1987.

Cloething, S., E. Burov, and A. Poliakov, Lithosphere folding: Primary response to compression?, *Tectonics*, *18*, 1064–1083, 1999.

Cooke, M. L., P. N. Mollema, D. D. Pollard, and A. Aydin, Interlayer slip and joint localization in the East Kaibab Monocline, Utah: Field evidence and results from numerical modelling, in *Forced Folds and Fractures*, edited by J. W. Cosgrove and M. S. Ameen, *Geol. Soc. Spec. Publ.*, *169*, 129–144, 2000.

Cortes, P., Mécanismes et caractérisation de la fracturation de mode 1 dans les roches stratifiés: terrain et expérimentation, Doctoral thesis, Univ. of Montpellier II, Montpellier, France, 2000.

Couples, G. D., and H. Lewis, Effects of interlayer slip in model forced folds, in *Forced Folds and Fractures*, edited by J. W. Cosgrove and M. S. Ameen, *Geol. Soc. Spec. Publ.*, *169*, 129–144, 2000.

Dalziel, I. W. D., and G. L. Stirewalt, Stress history of folding and cleavage development, Baraboo syncline, Wisconsin, *Geol. Soc. Am. Bull.*, *86*, 1671–1690, 1975.

Eshelby, J. D., The determination of the elastic field of an ellipsoidal inclusion, *Philos. Proc. R. Soc. London, Ser. A*, *241*, 376–396, 1957.

Gambarotta, L., and S. Lagomarsino, A microcrack damage model for brittle materials, *Solids Struct.*, *30*(2), 177–198, 1993.

Gholipour, A. M., Patterns and structural positions of productive fractures in the Asmari reservoirs, southwest Iran, *J. Can. Pet. Technol.*, *37*, 44–50, 1998.

Guiton, M. L. E., Contribution de la fracturation diffuse à la déformation d'ensemble durant le plissement de roches sédimentaires, thèse de Doctorat, Ecole Polytech., Palaiseau, France, 2001.

Guiton, M. L. E., W. Sassi, Y. M. Leroy, and B. D. M. Gauthier, Mechanical constraints on the chronology of fracture activation in folded Devonian sandstone of the western Moroccan Anti-Atlas, *J. Struct. Geol.*, in press, 2003.

Hennings, P. H., J. E. Olson, and L. B. Thompson, Combining outcrop data and three-dimensional structural models to characterize fractured reservoirs: An example from Wyoming, *AAPG Bull.*, *84*, 830–849, 2000.

Horii, H., and S. Nemat-Nasser, Brittle failure in compression: Splitting, faulting and brittle-ductile transition, *Philos. Trans. R. Soc. London, Ser. A*, *319*, 337–374, 1986.

Jamison, W. R., Quantitative evaluation of fractures on Monkshood anticline, a detachment fold in the foothills of western Canada, *AAPG Bull.*, *81*, 1110–1132, 1997.

Jeyakumaran, M., and J. W. Rudnicki, The sliding wing crack—Again!, *Geophys. Res. Lett.*, *22*(21), 2901–2904, 1995.

Kachanov, M. L., A microcrack model of rock inelasticity, part I, Frictional sliding on microcracks, *Mech. Mater.*, *1*, 19–27, 1982a.

Kachanov, M. L., A microcrack model of rock inelasticity, part II, Propagation of microcracks, *Mech. Mater.*, *1*, 29–41, 1982b.

Kachanov, M. L., Effective elastic properties of cracked solids: Critical review of some basic concepts, *Appl. Mech. Rev.*, *45*(8), 304–335, 1992.

Koiter, W. T., Stress-strain relations, uniqueness and variational theorem for elastic-plastic materials with a singular yield surface, *Q. Appl. Math.*, *11*, 350–354, 1953.

Leroy, Y. M., and W. Sassi, A plasticity model for discontinua, in *Aspects of Tectonic Faulting*, edited by F. K. Lehner and J. L. Urai, pp. 77–108, Springer-Verlag, New York, 2000.

Leroy, Y. M., and N. Triantafyllidis, Stability of a frictional, cohesive layer on a substratum: Variational formulation and asymptotic solution, *J. Geophys. Res.*, *101*, 17,795–17,811, 1996.

Leroy, Y. M., and N. Triantafyllidis, Onset of folding and faulting in density-stratified systems: An elastoplastic model, in *Aspects of Tectonic Faulting*, edited by F. K. Lehner and J. L. Urai, pp. 109–140, Springer-Verlag, New York, 2000.

Martinod, J., and P. Davy, Periodic instabilities during compression or extension of the lithosphere, 1, Deformation modes from an analytical perturbation method, *J. Geophys. Res.*, *97*, 1999–2014, 1992.

McAdoo, D. C., and D. T. Sandwell, Folding of the oceanic lithosphere, *J. Geophys. Res.*, *90*, 8563–8569, 1985.

McQuillan, H., Small-scale fracture density in Asmari formation of southwest Iran and its relation to bed thickness and structural setting, *AAPG Bull.*, *57*, 2367–2385, 1973.

Renshaw, C. E., Mechanical controls on the spatial density of opening-mode fracture networks, *Geology*, *25*, 923–926, 1997.

Rives, T., M. Razack, J.-P. Petit, and K. D. Rawnsley, Joint spacing: Analogue and numerical simulations, *J. Struct. Geol.*, *14*(8/9), 925–937, 1992.

Rudnicki, J. W., and J. R. Rice, Conditions for the localization of the deformation in pressure-sensitive dilatant materials, *J. Mech. Phys. Solids*, *23*, 371 – 394, 1975.

Sassi, W., and J. L. Faure, Role of faults and layer interfaces on the spatial variation of stress regime in basins: Inference from numerical modelling, *Tectonophysics*, *266*, 101 – 119, 1997.

Sassi, W., B. Colletta, P. Bale, and T. Paquereau, Modeling of structural complexity in sedimentary basins: The role of pre-existing faults in thrust tectonics, *Tectonophysics*, *226*, 143 – 166, 1993.

Sherwin, J. A., and W. N. Chapple, Wavelengths of single layer folds: A comparison between theory and observation, *Am. J. Sci.*, *266*, 167 – 179, 1968.

Sibson, R. H., A note on fault-reactivation, *J. Struct. Geol.*, *7*, 751 – 754, 1985.

Silliphant, L. J., T. Engelder, and M. Gross, The state of stress in the limb of the Split Mountain anticline, Utah: Constraints placed by transected joints, *J. Struct. Geol.*, *24*, 155 – 172, 2002.

Simo, J. C., and R. L. Taylor, Consistent tangent operators for rate-independent plasticity, *Comput. Math. Appl. Mech. Eng.*, *48*, 101 – 118, 1985.

Stören, S., and J. R. Rice, Localized necking in thin sheets, *J. Mech. Phys. Solids*, *23*, 421 – 441, 1975.

Triantafyllidis, N., and Y. M. Leroy, Stability of a frictional, cohesive layer on a substratum: Validity of asymptotic solution and influence of material properties, *J. Geophys. Res.*, *102*, 20,551 – 20,570, 1997.

Wallace, R. E., Geometry of shearing stress and relation to faulting, *J. Geol.*, *59*, 118 – 130, 1951.

Wallace, M. H., and H. J. Melosh, Buckling of a pervasively faulted lithosphere, *Pure Appl. Geophys.*, *142*, 239 – 261, 1994.

Walsh, J. B., The effects of cracks on the uniaxial elastic compression of rocks, *J. Geophys. Res.*, *70*, 399 – 411, 1965.

Withjack, M. O., and C. Scheiner, Fault patterns associated with domes—An experimental and analytical study, *AAPG Bull.*, *66*, 302 – 316, 1982.

M. L. E. Guiton and W. Sassi, Institut Français du Pétrole, Division Géologie-Géochimie, 1-4 Avenue de Bois-Préau, F-92852 Rueil-Malmaison Cedex, France. (martin.guiton@ifp.fr; william.sassi@ifp.fr)

Y. M. Leroy, Laboratoire de Mécanique des Solides, UMR 7649 CNRS, Ecole Polytechnique, F-91128 Palaiseau Cedex, France. (leroyy@lms.polytechnique.fr)